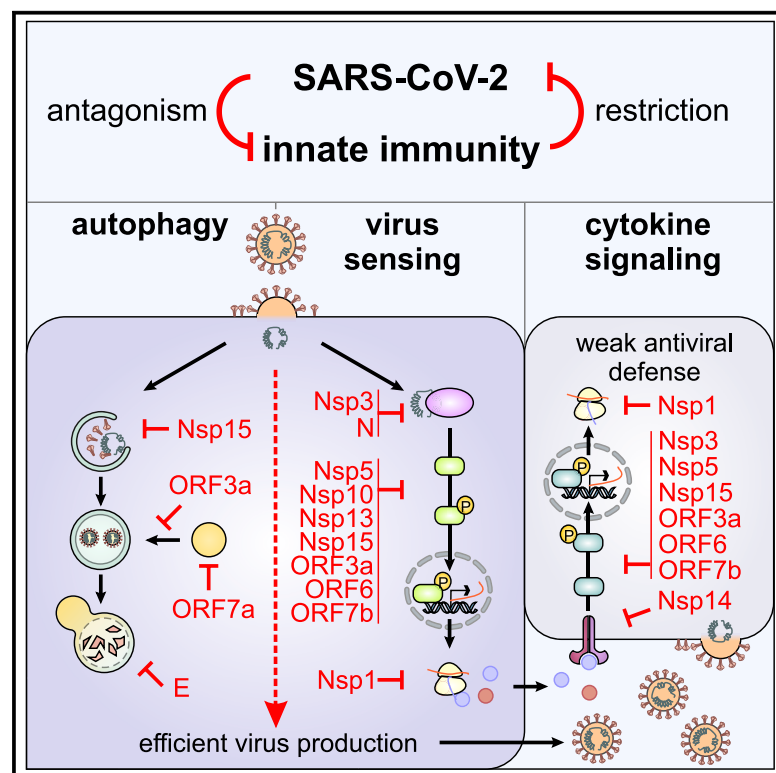


# Systematic functional analysis of SARS-CoV-2 proteins uncovers viral innate immune antagonists and remaining vulnerabilities

## Graphical abstract



## Authors

Manuel Hayn, Maximilian Hirschenberger, Lennart Koepke, ..., Axel Imhof, Frank Kirchhoff, Konstantin Maria Johannes Sparrer

## Correspondence

konstantin.sparrer@uni-ulm.de

## In brief

Hayn et al. analyze the impact of individual SARS-CoV-2 proteins on virus sensing, interferon signaling, and autophagy. They define the repertoire of viral antagonists of innate immune defenses, determine selected underlying mechanisms, and identify remaining vulnerabilities of SARS-CoV-2.

## Highlights

- Numerous SARS-CoV-2 proteins synergize to suppress immune sensing and signaling
- Nsp14 targets IFNAR1 for lysosomal degradation
- ORF3a and ORF7a block autophagy by different mechanisms
- Synergistic treatment with IFN- $\gamma$  and - $\lambda$ 1 is highly effective against SARS-CoV-2



## Article

# Systematic functional analysis of SARS-CoV-2 proteins uncovers viral innate immune antagonists and remaining vulnerabilities

Manuel Hayn,<sup>1,8</sup> Maximilian Hirschenberger,<sup>1,8</sup> Lennart Koepke,<sup>1,8</sup> Rayhane Nchioua,<sup>1</sup> Jan Hendrik Straub,<sup>1</sup> Susanne Klute,<sup>1</sup> Victoria Hunszinger,<sup>1</sup> Fabian Zech,<sup>1</sup> Caterina Prelli Bozzo,<sup>1</sup> Wasim Aftab,<sup>3,4</sup> Maria Hønholt Christensen,<sup>6</sup> Carina Conzelmann,<sup>1</sup> Janis Alexander Müller,<sup>1</sup> Smitha Srinivasachar Badarinarayan,<sup>1,7</sup> Christina Martina Stürzel,<sup>1</sup> Ignasi Forne,<sup>3</sup> Steffen Stenger,<sup>5</sup> Karl-Klaus Conzelmann,<sup>2</sup> Jan Münch,<sup>1</sup> Florian Ingo Schmidt,<sup>6</sup> Daniel Sauter,<sup>1,7</sup> Axel Imhof,<sup>3</sup> Frank Kirchhoff,<sup>1</sup> and Konstantin Maria Johannes Sparrer<sup>1,9,\*</sup>

<sup>1</sup>Institute of Molecular Virology, Ulm University Medical Center, 89081 Ulm, Germany

<sup>2</sup>Max von Pettenkofer-Institute of Virology, Medical Faculty, and Gene Center, Ludwig-Maximilians-Universität München, 81377 Munich, Germany

<sup>3</sup>Biomedical Center, Zentrallabor für Proteinanalytik (Protein Analysis Unit), Medical Faculty, Ludwig-Maximilians-Universität München, 82152 Planegg-Martinsried, Germany

<sup>4</sup>Graduate School for Quantitative Biosciences (QBM), Ludwig-Maximilians-University of Munich, 81377 Munich, Germany

<sup>5</sup>Institute for Medical Microbiology and Hygiene, Ulm University Medical Center, 89081 Ulm, Germany

<sup>6</sup>Institute of Innate Immunity, Medical Faculty, University of Bonn, 53127 Bonn, Germany

<sup>7</sup>Institute of Medical Virology and Epidemiology of Viral Diseases, University Hospital Tübingen, 72076 Tübingen, Germany

<sup>8</sup>These authors contributed equally

<sup>9</sup>Lead contact

\*Correspondence: [konstantin.sparrer@uni-ulm.de](mailto:konstantin.sparrer@uni-ulm.de)  
<https://doi.org/10.1016/j.celrep.2021.109126>

## SUMMARY

Severe acute respiratory syndrome coronavirus 2 (SARS-CoV-2) evades most innate immune responses but may still be vulnerable to some. Here, we systematically analyze the impact of SARS-CoV-2 proteins on interferon (IFN) responses and autophagy. We show that SARS-CoV-2 proteins synergize to counteract anti-viral immune responses. For example, Nsp14 targets the type I IFN receptor for lysosomal degradation, ORF3a prevents fusion of autophagosomes and lysosomes, and ORF7a interferes with autophagosome acidification. Most activities are evolutionarily conserved. However, SARS-CoV-2 Nsp15 antagonizes IFN signaling less efficiently than the orthologs of closely related RaTG13-CoV and SARS-CoV-1. Overall, SARS-CoV-2 proteins counteract autophagy and type I IFN more efficiently than type II or III IFN signaling, and infection experiments confirm potent inhibition by IFN- $\gamma$  and - $\lambda$ 1. Our results define the repertoire and selected mechanisms of SARS-CoV-2 innate immune antagonists but also reveal vulnerability to type II and III IFN that may help to develop safe and effective anti-viral approaches.

## INTRODUCTION

The severe acute respiratory syndrome coronavirus 2 (SARS-CoV-2) is a zoonotic, novel coronavirus that emerged at the end of 2019 (Andersen et al., 2020; Wu et al., 2020; Zhou et al., 2020a). Infection with SARS-CoV-2 causes coronavirus disease 2019 (COVID-19) (Huang et al., 2020). The virus rapidly spread all over the world owing to its higher transmission rates (Ferretti et al., 2020), as well as a lower morbidity and case fatality rates (CFRs; 3%–4%) (WHO, 2020) than those of previous epidemic coronaviruses such as SARS-CoV-1 (CFR, 11%) or middle east respiratory syndrome coronavirus (MERS-CoV; CFR, 35%) (Chan-Yeung and Xu, 2003; Petersen et al., 2020; Zumla et al., 2015). However, its pathogenicity is still much higher than that of “common cold” CoVs such as HKU1 and 229E (Corman et al., 2018), and to date, SARS-CoV-2 has

caused more than 3 million deaths (<https://coronavirus.jhu.edu/map.html>).

Upon infection of a target cell, CoVs may be recognized by innate immune sensors like RIG-like receptors (RLRs) (Kell and Gale, 2015). Subsequently, these activate cell-intrinsic innate immune defenses (hereafter referred to as the innate immune system) (Frieman et al., 2008; Totura and Baric, 2012), such as interferon (IFN) responses and autophagy (Takeuchi and Akira, 2009). Activation of RLRs induces signaling cascades that ultimately lead to the release of IFNs and other pro-inflammatory cytokines as well as induction of anti-viral effectors (Koepke et al., 2021). Released IFNs and other cytokines are subsequently also recognized by neighboring cells to induce an anti-viral transcriptional response and eventually limit viral spread (van Gent et al., 2018; Sparrer and Gack, 2015). Besides cytokine-mediated signaling cascades, other mechanisms that are able to directly



eliminate invading pathogens are activated, such as autophagy. Autophagy is capable of targeting viral components or even whole viruses for lysosomal degradation (Choi et al., 2018; Sparrer et al., 2017; Sparrer and Gack, 2018). Eventually, activation of innate immunity recruits and stimulates the adaptive immune system, ultimately facilitating elimination of the virus (Iwasaki and Medzhitov, 2010, 2015). Inborn defects in innate immunity or auto-antibodies against IFNs are associated with high frequencies of severe COVID-19, suggesting that innate defense mechanisms play a major role in immune control of SARS-CoV-2 (Bastard et al., 2020; Zhang et al., 2020). Notably, SARS-CoV-2 infections show higher numbers of subclinical infections (up to 80%; WHO, 2020) than previous epidemic CoVs such as SARS-CoV-1 (Corman et al., 2018). Indeed, recent evidence suggests that SARS-CoV-2 is more sensitive toward IFNs than SARS-CoV-1 *in vitro* (Lokugamage et al., 2020). However, the underlying reasons for differences in IFN susceptibility between SARS-CoV-2 and SARS-CoV-1 are poorly understood.

Recent reports suggest that SARS-CoV-2 manipulates the innate immune response (Blanco-Melo et al., 2020; Stukalov et al., 2020). For example, ORF3b antagonizes type I IFN induction by a yet unknown mechanism (Konno et al., 2020). In addition, the SARS-CoV-2 non-structural protein 1 (Nsp1) shuts down cellular translation including the cytokine-mediated innate immune response (Schubert et al., 2020; Thoms et al., 2020). Analysis of the interplay between SARS-CoV-2 proteins and IFN- $\beta$  induction and signaling revealed that at least 8 of the about 30 SARS-CoV-2 proteins interfere with type I IFN signaling (Lei et al., 2020; Xia et al., 2020). However, so far only type I IFN signaling was analyzed in some detail, and our knowledge of how SARS-CoV-2 manipulates innate immunity is far from being complete.

Currently, IFN treatment is being explored in clinical trials against SARS-CoV-2 (Fragkou et al., 2020; Sallard et al., 2020). Studies assessing the effects of type I IFNs, often in combination with anti-viral treatment, show promising results (Huang et al., 2020; Hung et al., 2020; Shalhoub, 2020; Thorlund et al., 2020; Wang et al., 2020; Zhou et al., 2020b). However, patients receiving IFN therapy often suffer from severe side effects including psychological symptoms such as depression (Fried, 2002; Neri et al., 2010; van Zonneveld et al., 2005). Novel strategies that activate the immune system in a manner that is highly effective against SARS-CoV-2 while minimizing overall inflammation and detrimental effects are needed (Hung et al., 2020). Thus, understanding how SARS-CoV-2 antagonizes innate immunity may give valuable clues about viral vulnerabilities that might be exploited for safe and effective therapeutic immune control.

Here, we systematically analyzed the impact of 29 of the total 30 SARS-CoV-2-encoded proteins (Gordon et al., 2020; Hachimi et al., 2020) on the following major branches of the cell-intrinsic innate immune system: IFN induction, IFN/pro-inflammatory cytokine signaling, and autophagy. Our results identified Nsp1, Nsp3, Nsp5, Nsp10, Nsp13, Nsp14, ORF3a, ORF6, ORF7a, and ORF7b as major innate immune antagonists encoded by SARS-CoV-2. Interference with innate immune activation is achieved by diverse, synergistic mechanisms ranging from downregulation of IFN receptor (IFNAR1) expression by Nsp14

to blockage of autophagy by ORF3a and ORF7a, by interference with autophagosome-lysosome fusion or acidification of autophagosomes, respectively. The function of major innate immune antagonists was conserved between SARS-CoV-1, SARS-CoV-2, and the closely related bat RaTG13-CoV, with the following one notable exception: Nsp15 of SARS-CoV-2 is significantly less potent in suppressing IFN responses. Altogether, our analyses revealed that IFN- $\gamma$  and IFN- $\lambda$ 1 pathways are antagonized the least. Consequently, these two cytokines were most effective against SARS-CoV-2. A combined IFN- $\gamma$  and IFN- $\lambda$ 1 treatment at very low doses potentiated the individual anti-viral effect and could be further improved by anti-inflammatory autophagy activation.

## RESULTS

### A variety of SARS-CoV-2 proteins antagonize innate immune pathways

To systematically examine how SARS-CoV-2 manipulates innate immunity, we used Strep II-tagged expression constructs coding for 28 of the 30 currently known SARS-CoV-2 proteins (Nsp1, Nsp2, Nsp4, Nsp5, Nsp6, Nsp7, Nsp8, Nsp9, Nsp10, Nsp11, Nsp12, Nsp13, Nsp14, Nsp15, Nsp16, S, ORF3a, ORF3c, E, M, ORF6, ORF7a, ORF7b, ORF8, ORF9b, N, ORF9c, and ORF10) (Figure 1A). In addition, we examined untagged Nsp3. Expression of all proteins was confirmed by western blotting and immunofluorescence analyses (Figures S1A and S1B). The impact of all 29 viral proteins on 3 major branches of innate immunity, i.e., IFN/pro-inflammatory cytokine induction by RLRs (Figures 1B and S1C), signaling (Figures 1C and S1D), and autophagy (Figures 1D and S1E), was analyzed by quantitative reporter assays. All assays were normalized for cell viability (Figure S1F).

Induction of type I IFNs (IFN- $\alpha$  and IFN- $\beta$ ) was monitored using a firefly luciferase reporter controlled by the full IFN- $\alpha$ 4 and IFN- $\beta$  promoters (IFNA4 and IFNB1) or by isolated binding sites for the transcription factors IRF3 or nuclear factor  $\kappa$ B (NF- $\kappa$ B) (Figure 1B). HEK293T cells were infected with Sendai virus, mimicking RLR activation by SARS-CoV-2. Activity of type I IFN promoters, IRF3 binding sites, and NF- $\kappa$ B binding sites were strongly impaired by Nsp1, Nsp3, Nsp5, Nsp10, Nsp13, ORF6, and ORF7b (Figure 1B). Stimulation with type I and III IFNs, such as IFN- $\alpha$ 2, IFN- $\beta$ , and IFN- $\lambda$ 1, culminates in the induction of genes containing IFN response element (ISRE) promoters (Sparrer and Gack, 2015). Type II IFN- $\gamma$  causes activation of gamma activated sequence (GAS)-containing promoters. Pro-inflammatory cytokine signaling (tumor necrosis factor alpha [TNF- $\alpha$ ] and IL-1 $\alpha$ ) induces genes containing NF- $\kappa$ B sites in their promoter. Signaling of type I IFNs (IFN- $\alpha$ 2 and IFN- $\beta$ ), type II IFN (IFN- $\gamma$ ), type III IFN (IFN- $\lambda$ 1), and pro-inflammatory cytokine signaling (TNF- $\alpha$  and IL-1 $\alpha$ ) was quantified using quantitative firefly luciferase reporters controlled by the respective promoters (Figure S1D). Stimulation with IFN- $\alpha$ 2 and IFN- $\beta$  or pro-inflammatory cytokines revealed that activation of the ISRE and the NF- $\kappa$ B promoter is strongly repressed by Nsp1, Nsp5, Nsp13, Nsp14, ORF6, and ORF7b (Figures 1C and S1D). A similar set of viral proteins interfered with type II IFN- $\gamma$  and type III IFN- $\lambda$ 1 signaling (Figures 1C and S1D). Notably, the

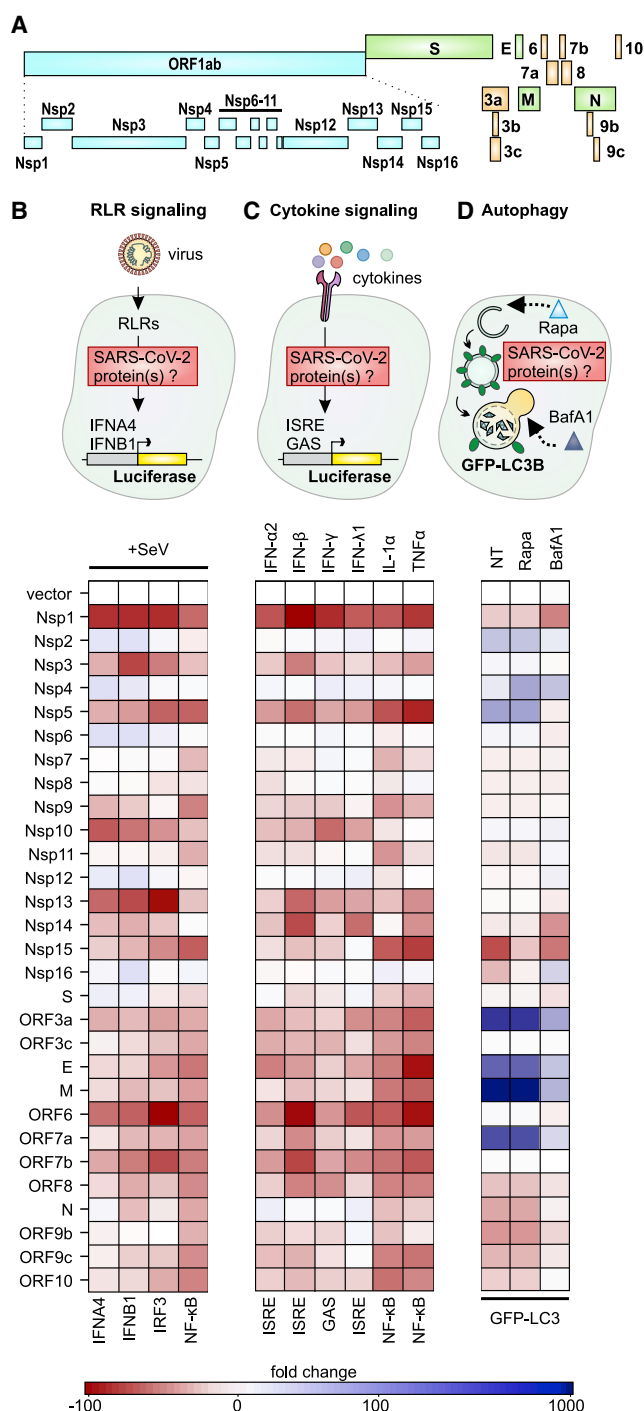


**Figure 1. Systematic analysis of innate immune antagonism by SARS-CoV-2 proteins**

(A) Schematic depiction of 30 SARS-CoV-2-encoded proteins in the order they appear in the genome. The polyprotein ORF1ab is (auto)proteolytically cleaved into 16 non-structural proteins (Nsps; turquoise). The structural proteins (green) are Spike (S), Membrane (M), envelope (E), and nucleoprotein (N). The set is complemented by the accessory proteins (orange) ORF3a, ORF3b, ORF3c, ORF6, ORF7a, ORF7b, ORF8, ORF9b, ORF9c, and ORF10.

(B–D) Schematic depiction of the assay setup (top panel) and heatmap (lower panel; red = inhibition, blue = induction) showing modulation of innate immune

average remaining activity of the signaling pathway, calculated as the aggregated mean of the signaling activity left in the presence of the individual viral proteins, showed differences in the efficiency by which these pathways are antagonized (Figure 1C). Type II and III IFN signaling are antagonized less (average remaining pathway activity of 82% and 89%, respectively) than type I IFN signaling (average remaining pathway activity of 22% for IFN-α2 and 47% for IFN-β).

Autophagy levels were monitored in SARS-CoV-2-protein-expressing HEK293T cells by membrane association of stably expressed GFP-LC3B (Figures 1D and S1E). During autophagy, cytoplasmic MAP1LC3B (LC3B) is proteolytically processed and lipidated (LC3B-II) to decorate autophagosomal membranes (Klionsky et al., 2016; Koepke et al., 2020). Autophagosome numbers under basal conditions were strongly increased in the presence of ORF3a, E, M, and ORF7a, suggesting either *de novo* induction of autophagy or blockage of turnover (Figure 1D). To differentiate between those processes, we treated cells with saturating amounts of Bafilomycin A1, which inhibits autophagic turnover. The increase of autophagosome numbers by ORF3a, E, M, and ORF7a was reduced compared to non-blocking conditions (Figure 1D), indicating that these proteins block turnover, rather than induce it. Blockage of autophagy and co-expression of Nsp1 and Nsp14 induced cell death, which may be responsible for the low number of autophagosomes. Unexpectedly, in the presence of Nsp15, autophagosome numbers were consistently reduced, suggesting that Nsp15 inhibits autophagy (Figure 1D).

Taken together, our analysis revealed a set of SARS-CoV-2 proteins that strongly antagonize cytokine induction (Nsp1, Nsp3, Nsp5, Nsp10, Nsp13, ORF6, and ORF7b), signaling (Nsp1, Nsp5, Nsp13, Nsp14, ORF6, and ORF7b), and autophagy (Nsp15, ORF3a, E, M, and ORF7a).

### SARS-CoV-2 proteins target type I IFN signaling at multiple levels

To analyze by which mechanisms type I IFN and autophagy are counteracted by SARS-CoV-2, we aimed at identifying the steps that are targeted in these pathways. We focused on the top five inhibitors according to Figures 1C and 1D. Nsp1 was removed from the analysis, as it prevents translation in general (Thoms et al., 2020). To analyze IFN-β signaling, we monitored the levels of the type I IFN receptor IFNAR1 by using western blotting in HEK293T cells overexpressing Nsp5, Nsp13, Nsp14, ORF6, or ORF7b. Activation of the two major transcription factors of type I IFN signaling, namely, STAT1 and STAT2 (Figure 2A), was examined by phosphorylation status. Basal STAT1 and STAT2 levels were not significantly affected by any of the

pathways by overexpression of indicated SARS-CoV-2 proteins. Stimuli of the respective pathways are indicated. (B and C) Readout by Luciferase reporter gene assay (color represents the mean of  $n = 3$ , biological replicates) using indicated promoter constructs in HEK293T cells, and (D) autophagosome measurement by quantification of membrane-associated GFP-LC3B in HEK293T-GFP-LC3B cells (color represents the mean of  $n = 4$ , biological replicates). The vector/control is set to 1 (white). SeV, Sendai virus; Rapa, rapamycin; BafA1, Bafilomycin A1. Heatmaps represent one example of at least two independent repeats, each consisting of three biological replicates. See also Figure S1.



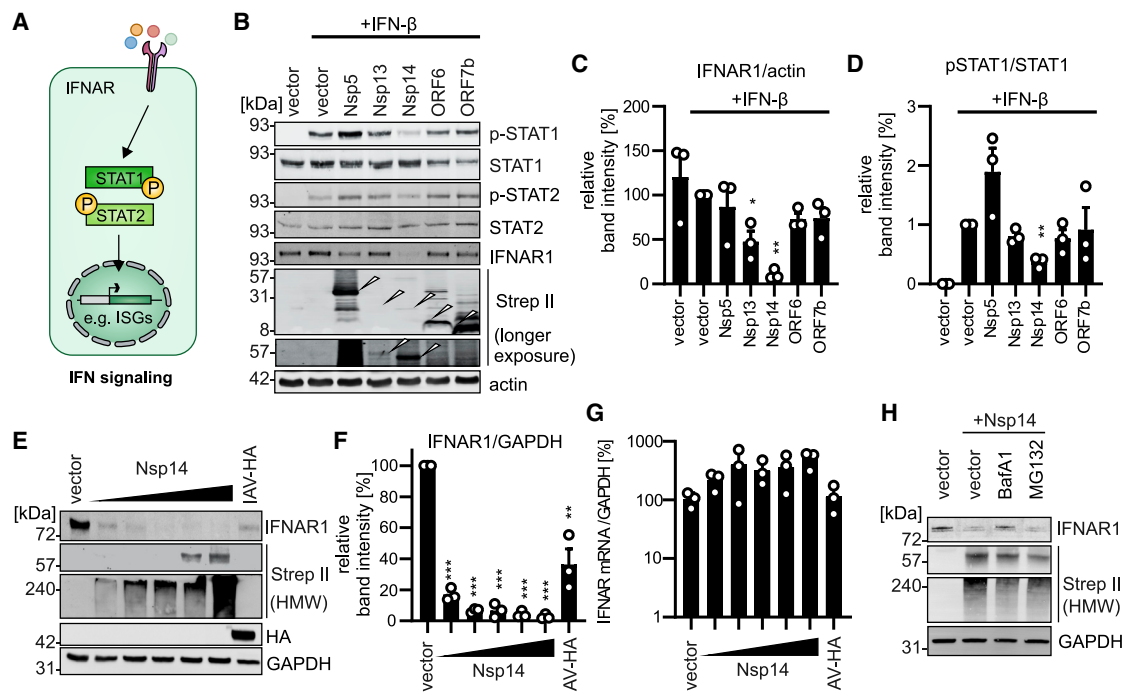


**Figure 2. SARS-CoV-2 interferes with type I IFN signaling**

(A) Schematic depiction of the type I IFN signaling pathway.

(B) Exemplary immunoblot analysis showing activation of type I IFN signaling markers by using whole-cell lysates (WCLs) of HEK293T cells expressing indicated proteins and stimulated with IFN-β (1000 U/mL, 45 min). Blots were stained with anti-pSTAT1, anti-STAT1, anti-pSTAT2, anti-STAT2, anti-IFNAR1, anti-Strep II, and anti-actin. (C) Quantification of the band intensities in (B) for IFNAR1 normalized to the band intensities of actin. Bars represent mean of  $n = 3 \pm \text{SEM}$  (biological replicates). (D) Quantification of the band intensities in (B) for phospho-STAT1 (pSTAT1) normalized to the band intensities of STAT1. Bars represent the mean of  $n = 3 \pm \text{SEM}$  (biological replicates).

(E) Exemplary immunoblot analysis showing endogenous levels of IFNAR1 in WCLs of HEK293T cells expressing indicated proteins. Blots were stained with anti-IFNAR1, anti-Strep II, anti-HA, and anti-GAPDH. IAV-HA, HA-tagged influenza virus HA protein.

(F) Quantification of the band intensities in (E) for IFNAR1 normalized to the band intensities of GAPDH. Bars represent the mean of  $n = 3 \pm \text{SEM}$  (biological replicates).

(G) Quantitative real-time PCR analysis of IFNAR1 mRNA levels in HEK293T cells expressing indicated proteins, normalized to GAPDH mRNA. Vector transfected samples were set to 100%. Bars represent the mean of  $n = 3 \pm \text{SEM}$  (biological replicates).

(H) Exemplary immunoblot analysis showing endogenous levels of IFNAR1 in WCLs of HEK293T cells expressing Nsp14. Cells were treated with BafA1 (2  $\mu\text{M}$ ) or MG132 (50  $\mu\text{M}$ ) for 6 h before harvesting. Blots were stained with anti-IFNAR1, anti-Strep II, and anti-GAPDH.

\*,  $p < 0.05$ ; \*\*,  $p < 0.01$ ; \*\*\*,  $p < 0.001$ . See also Figure S2.

proteins tested (Figure 2B; quantification in Figures S2A and S2B). In the presence of Nsp5, activated STAT1 accumulates (Figures 2B and 2D). A similar tendency is also observed for phospho-STAT2 (Figure S2C). Neither ORF6 nor ORF7b affected IFNAR1 levels or STAT1 expression and activation (Figures 2B–2D and S2B). This finding agrees with recent reports (Kimura et al., 2021; Lei et al., 2020; Yuen et al., 2020) suggesting that ORF6 prevents the trafficking of transcription factors. In the presence of Nsp14 and (to a lesser extent) Nsp13, endogenous levels of IFNAR1 were significantly reduced (Figures 2B and 2C). Consequently, phosphorylation of STAT1 was decreased upon Nsp14 overexpression (Figures 2B and 2D). Expression of Nsp14 specifically induced degradation of endogenous IFNAR1 at the protein level (Figures 2E and 2F), as the mRNA levels of IFNAR1 remained unchanged or are even increased in the presence of Nsp14 (Figure 2G). Notably, Nsp14 seems to be modified by post-translational modifications, as high-molecular-weight isoforms are detectable (HMW; Figure 2E). Influenza virus hem-

agglutinin (HA) was used as a positive control (Xia et al., 2016). Inhibition of lysosomal degradation by Bafilomycin A1 in the absence of Nsp14 did not affect endogenous IFNAR1 levels (Figure S2D). However, in the presence of Nsp14, IFNAR1 levels were rescued by the addition of Bafilomycin A1, indicating that lysosomal activity is required for Nsp14-mediated degradation of IFNAR1 (Figure 2H).

Taken together, our data demonstrate that the major type I IFN antagonists of SARS-CoV-2, namely, Nsp5, Nsp13, Nsp14, ORF6, and ORF7b, block the signaling cascade at different levels. Mechanistically, Nsp14 induces lysosomal degradation of the essential receptor of type I IFNs, namely, IFNAR1, thereby preventing STAT transcription factor activation.

### SARS-CoV-2 proteins interfere with autophagy

Upon fusion of LC3B-II decorated autophagosomes with lysosomes, the autophagic receptor p62 is degraded (autophagic turnover; Figure 3A). We analyzed the effect of the top 5

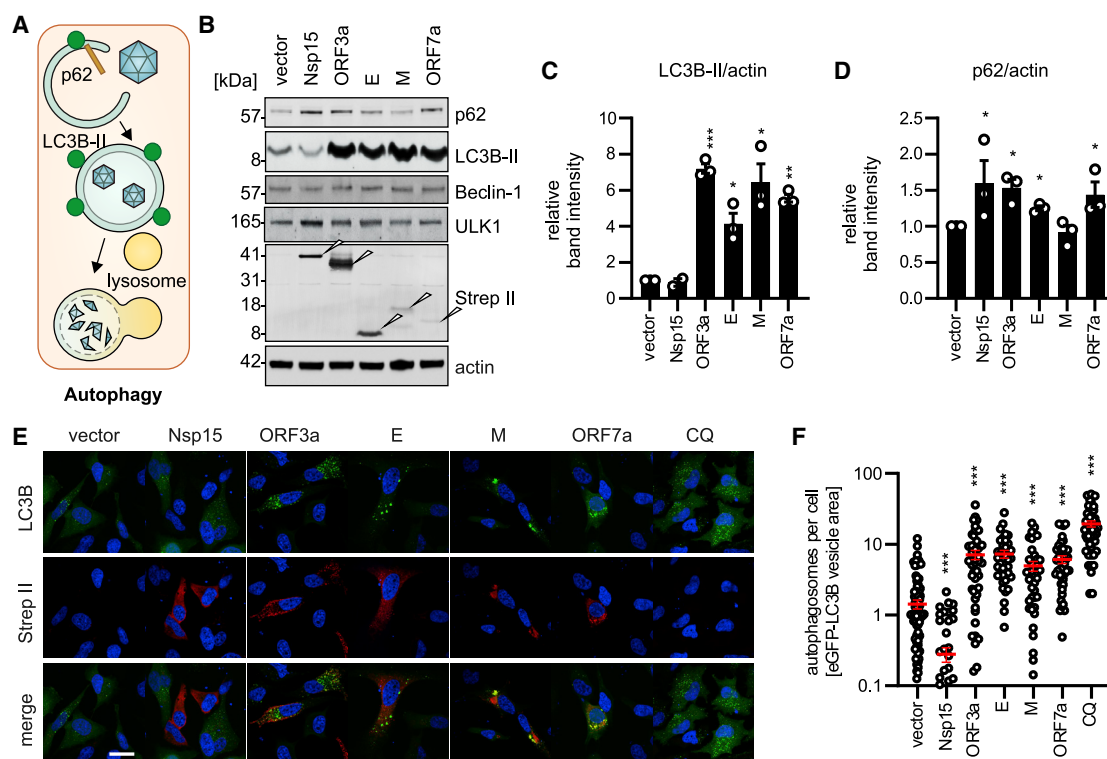


**Figure 3. SARS-CoV-2 interferes with autophagy**

(A) Schematic depiction of autophagy.

(B) Exemplary immunoblot analysis showing autophagy activity markers using WCLs of HEK293T cells expressing indicated proteins. Blots were stained with anti-SQSTM1/p62, anti-LC3B-II, anti-Beclin-1, anti-ULK1, anti-Strep II, and anti-actin.

(C) Quantification of the band intensities in (B) for LC3B-II normalized to the band intensities of actin. Bars represent mean of  $n = 2-3 \pm \text{SEM}$  (biological replicates).

(D) Quantification of the band intensities in (B) for p62 normalized to the band intensities of actin. Bars represent mean of  $n = 3 \pm \text{SEM}$  (biological replicates).

(E) Exemplary confocal laser scanning microscopy images of autophagy activation by GFP-LC3B (green) puncta formation. Indicated Strep II-tagged SARS-CoV-2 proteins (red) were overexpressed in HeLa GFP-LC3B cells (green). CQ (chloroquine; 4 h, 10  $\mu\text{M}$ ) was used as a positive control. Nuclei, 4',6-diamidino-2-phenylindole (DAPI; blue). Scale bar, 25  $\mu\text{m}$ .

(F) Quantification by area of GFP-LC3B puncta divided by cell number from the images in (E). Bars represent the mean of  $n = 38-100 \pm \text{SEM}$  (individual cells).

\*,  $p < 0.05$ ; \*\*,  $p < 0.01$ ; \*\*\*,  $p < 0.001$ . See also Figure S2.

autophagy-modulating SARS-CoV-2 proteins, namely, Nsp15, ORF3a, E, M, and ORF7a, on autophagy markers (Figure 1D). Levels of beclin-1 and ULK1, which are parts of the core machinery of autophagy initiation, remained constant (Figures 3B, S2E, and S2F). Overexpression of Nsp15 led to a slight but consistent decrease of LC3B-II and accumulation of p62, suggesting that Nsp15 blocks induction of autophagy (Figures 3C and 3D). In line with this finding, the number of GFP-LC3B-puncta (= autophagosomes) per cell in HeLa GFP-LC3B cells was reduced upon Nsp15 expression to almost 0 (Figures 3E and 3F). In the presence of ORF3a, E, or ORF7a, the levels of processed LC3B (LC3B-II) were 4- to 7-fold increased (Figure 3C), whereas p62 levels were approximately 1.5-fold increased (Figure 3D). This result indicates that these three viral proteins block autophagic turnover. Thus, the number of autophagosomes per cell was 10-fold increased upon ORF3a, E, or ORF7a expression (Figures 3E and 3F). Curiously, although accumulation of LC3B-II indicates that M blocks autophagic turnover or induces autophagy, the levels of p62 were not significantly altered in the presence of M (Figures 3B–3D). Notably, overexpression of M re-

sulted in an accumulation of LC3B in the perinuclear space, whereas for all other viral proteins autophagosomes were normally distributed (Figures 3E and 3F). As Nsp15 reduced the number of autophagosomes, whereas three different proteins led to accumulation of autophagosomes, we asked which phenotype is dominant during SARS-CoV-2 infection. Both in Calu-3 and Caco-2 cells infected for 48 h with SARS-CoV-2, the levels of p62 and processed LC3B were increased (Figures S2G and S2H) suggesting that autophagic turnover is blocked during the infection.

Our data demonstrate that SARS-CoV-2 E, ORF3a, and ORF7a block autophagic turnover, whereas M may differently interact with the autophagic machinery and Nsp15 inhibits *de novo* autophagy induction. In the viral context, autophagic flux is blocked.

#### ORF3a and ORF7a prevent autophagosome acidification by perturbing the autophagosome-lysosome interplay

Our data show that ORF3a and ORF7a are the most potent autophagy antagonists of SARS-CoV-2 (Figures 1D and 3B–3F). To

determine their molecular mechanism(s), we performed proteome analysis of HEK293T cells overexpressing SARS-CoV-2 ORF3a and ORF7a (Figure S3A). As controls, we used cells overexpressing S, Nsp1, and Nsp16, which showed little to no effect on autophagy (Figure 1D). In addition, we analyzed the proteome of Caco-2 cells infected with SARS-CoV-2 for 24 or 48 h. Fold changes compared to vector-transfected or non-infected controls were calculated (Figures 4A, 4B, and S3B–S3E; Table S1). We found that cellular proteins with a short half-life are markedly reduced in the presence of Nsp1 (Figure S3F; Mathieson et al., 2018). This agrees with our previous finding that Nsp1 globally blocks translation (Thoms et al., 2020). PANTHER-assisted Gene Ontology analysis of the proteins regulated more than 4-fold by overexpression of individual SARS-CoV-2 proteins revealed that ORF3a and ORF7a target the late endosome pathway (Gene Ontology: 0005770) (Figure 4C; Table S2). A similar analysis for samples obtained after virus infection showed that the late endosome pathway is also affected during genuine SARS-CoV-2 infection. In line with the proteome analysis, ORF7a and ORF3a both localized to the late endosomal compartment, co-localizing with the marker Rab9 (Figures 4D and 4E). In contrast, localization to Rab5a-positive early endosomes was not apparent (Figure S3G). Disturbance of the integrity of the *trans*-Golgi network (TGN) at the interface with the late endosomes (Brandizzi and Barlowe, 2013; Progidia and Bakke, 2016) is an additional indicator for defects in autophagy (Hansen et al., 2017). Immunofluorescence analysis revealed that the localization of ORF3a or ORF7a only partially overlaps with a TGN marker ( $R = \sim 0.5$ ; Figures S4A and S4B). ORF6 and Nsp8 were used as positive and negative control ( $R = \sim 0.7$ ,  $R = \sim 0.3$ ), respectively (Lei et al., 2020). Importantly, analysis of free TGN-marker-positive vesicles in SARS-CoV-2 ORF3a or ORF7a expressing cells revealed that both viral proteins cause significant fragmentation of the TGN (Figures 4F and S4A). Thus, we asked whether ORF3a or ORF7a alters autophagosome-lysosome dynamics. To this end, we used an mCherry-GFP-LC3B double reporter system (Klionsky et al., 2016) that allows us to assess the acidity of autophagosomes relying on the instability of GFP at low pH. An increased ratio between GFP and mCherry (Figures 4G, S4C, and S4D) suggested that both ORF3a and ORF7a prevent the acidification of autophagosomes. This finding indicates that either the pH of lysosomes is altered or autophagosomal-lysosomal fusion is prevented. We assessed the acidity of lysosomes by using a pH-dependent lysotracker (Figure 4H) and lysosomal-autophagosomal fusion by colocalization of the lysosomal marker LAMP1 and the autophagosome marker LC3B (Figures 4I and 4J). Expression of ORF3a in HEK293T cells increased the signal of acidic lysosomes (Figure 4H), whereas co-localization of autophagosomes and lysosomes in ORF3a expressing HeLa GL cells is decreased (Figures 4I and 4J;  $R = \sim 0.42$ ) compared to the vector control ( $R = \sim 0.5$ ). ORF7a on the other hand showed increased LAMP1/LC3B co-localization (Figures 4I and 4J;  $R = \sim 0.6$ ) compared to the vector control ( $R = \sim 0.5$ ). However, the acidity of lysosomes, similar to the control Bafilomycin A1, was decreased (Figure 4H). Thus, ORF7a prevents autophagic degradation by altering the pH of lysosomes.

These data indicate that ORF3a and ORF7a disturb the proteome at the late endosomes, eventually leading to blockage of

autophagy by the following two distinct mechanisms: ORF3a stops the fusion of lysosomes and autophagosomes, while ORF7a reduces the acidity of lysosomes.

### SARS-CoV-2 Nsp15 is less potent in innate immune antagonism than SARS-CoV-1 Nsp15

To examine the conservation of innate immune antagonism activities, we functionally compared Nsp1, Nsp3, Nsp7, Nsp15, M, N, ORF3a, ORF6, and ORF7a of SARS-CoV-2, the closely related bat CoV RaTG13-CoV and the previous highly pathogenic SARS-CoV-1. RaTG13-CoV was isolated from horseshoe bats (*Rhinolophus affinis*), a putative reservoir host. Western blot analysis confirmed the expression of all constructs (Figures S5A–S5I). Rabies virus P protein (RABV P), measles virus V protein (MeV V), and TRIM32 expression served as positive controls. Quantitative PCR (qPCR) on endogenous IFNB1 mRNA and ELISA detecting secreted IFN- $\beta$  confirmed the results of the reporter gene assays (Figures S5J and S5K). Overall, proteins of SARS-CoV-1 and RaTG13-CoV impacted type I IFN induction, type I IFN signaling, and autophagy similar to their SARS-CoV-2 counterparts (Figures 5A–5C). However, this was not the case for Nsp15, Nsp3, and (to a lesser extent) ORF6 (Figures 5A–5C). Expression levels of SARS-CoV-1 ORF6 were also higher than those of its SARS-CoV-2 and RaTG13-CoV counterparts (Figure S5G), which may explain the differences in activity. Differences between SARS-CoV-1, RaTG13-CoV, and SARS-CoV-2 Nsp3 were reanalyzed in a dose-dependent manner, ranging only between 2- and 3-fold (Figure S5L). The most striking difference was observed for Nsp15. Notably, expression levels of SARS-CoV-2, RaTG13-CoV and SARS-CoV-1 Nsp15 were comparable (Figure S5C). All Nsp15 variants still inhibited autophagy (Figure 5C). Dose-dependent analyses showed that SARS-CoV-2 Nsp15 counteracted type I IFN induction on average 32-fold or 7.8-fold less potently than SARS-CoV-1 or RaTG13-CoV Nsp15, respectively (Figures 5D and S5M). In line with this result, SARS-CoV-1 Nsp15 outperformed RaTG13-CoV and SARS-CoV-2 Nsp15 by 15- and 5.7-fold, respectively, in suppressing type I IFN signaling (Figures 5E and S5N).

Altogether, our results show that although most IFN antagonism activities are conserved between SARS-CoV-1, RaTG13-CoV, and SARS-CoV-2, there is one exception, namely, Nsp15 of SARS-CoV-1 is considerably more potent than SARS-CoV-2 Nsp15 in counteracting both IFN- $\beta$  induction and signaling.

### Efficiency of the antagonism of SARS-CoV-2 proteins correlates inversely with virus inhibition

Our analyses revealed that several SARS-CoV-2 proteins synergize to antagonize innate immune activation pathways, albeit with different efficiencies. Consequently, we determined whether IFN- $\alpha$ 2, IFN- $\beta$ , IFN- $\gamma$ , and IFN- $\lambda$ 1 inhibit SARS-CoV-2 with different efficiencies (Figures 6A and 6B; Figures S6A and S6B). Treatment with type I IFN- $\alpha$ 2 was least efficient. In contrast, at the same concentration, type II IFN- $\gamma$  (500 U/mL) reduced viral RNA in the supernatant almost 300-fold more efficiently. At low concentrations (5 U/mL) the type II and III IFNs were most active against SARS-CoV-2, which was confirmed by Median Tissue Culture Infectious Dose (TCID<sub>50</sub>) analysis of the infectious particles released (Figures 6A and 6B). All agents

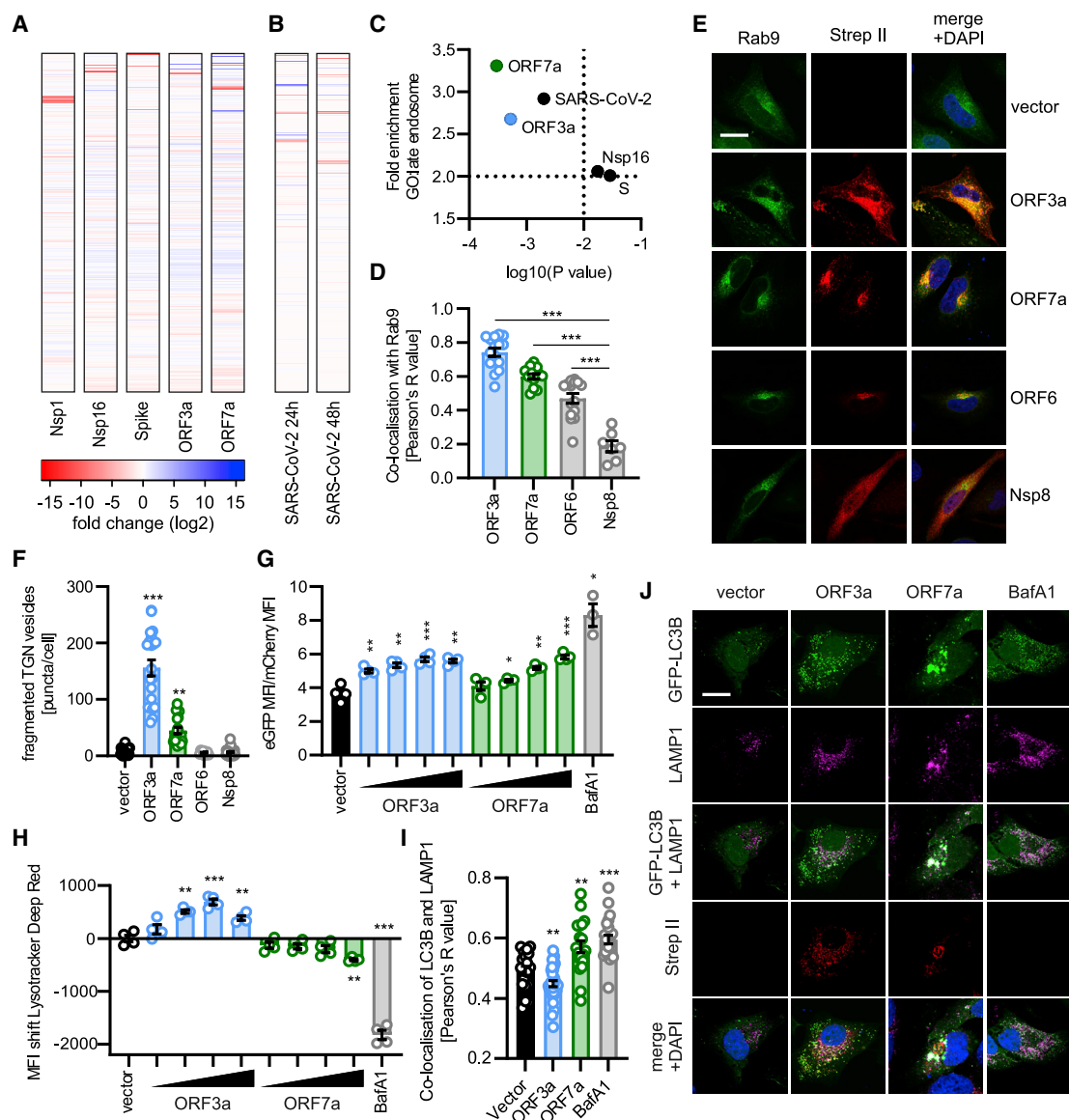


**Figure 4. ORF3a and ORF7a disturb autophagy by distinct mechanisms**

(A and B) Heatmap (red = downregulation, blue = upregulation) depicting the fold changes of cellular and viral proteins during overexpression of indicated single SARS-CoV-2 proteins in HEK293T cells (A) or SARS-CoV-2 infection (MOI, 1) of Caco-2 cells 24 h or 48 h post-infection as assessed by mass spectrometry (B). (C) Scatterplots of log2 fold enrichment and p value of the GO term "late endosome" in protein sets regulated more than 4-fold upon (A) expression of indicated viral protein or (B) SARS-CoV-2 infection.

(D) Quantification of co-localization by Pearson correlation of Rab9 and indicated viral proteins in HeLa cells transiently transfected with the indicated viral protein and GFP-Rab9. Bars represent the mean of  $n = 7-15 \pm \text{SEM}$  (individual cells).

(E) Exemplary confocal microscopy images of HeLa cells transiently expressing indicated viral proteins (red) and a marker of late endosomes GFP-Rab9 (green). Cells were stained with anti-Strep II (red). Nuclei, DAPI (blue). Scale bar, 10  $\mu\text{m}$ .

(F) Quantification of non-Golgi-associated vesicles per cell as puncta/cell in HeLa cells overexpressing indicated proteins. Images in Figure S4A. Bars represent the mean of  $n = 15-25 \pm \text{SEM}$  (individual cells).

(G) Ratio between eGFP and mCherry mean fluorescence intensities in HEK293T stably expressing GFP-mCherry-LC3B and transfected with indicated constructs. BafA1 at 100 nM, 8 h. Bars represent the mean of  $n = 4 \pm \text{SEM}$  (biological replicates).

(H) Mean fluorescence intensity of LysoTracker-deep-red-stained HEK293T cells expressing indicated proteins, as assessed by flow cytometry. Bars represent the mean of  $n = 4 \pm \text{SEM}$  (biological replicates).

(I) Quantification of the co-localization of LAMP1 and LC3B in HeLa-GFP-LC3B cells expressing indicated proteins. Bars represent the mean of  $n = 19-32 \pm \text{SEM}$  (individual cells).

(J) Exemplary confocal microscopy images for (I). Cells were stained with anti-Strep II (red) and anti-LAMP1 (magenta). GFP-LC3B, green. Nuclei, DAPI (blue). Scale bar, 10  $\mu\text{m}$ . BafA1 (100 nM, 4 h) was used as a positive control.

\*,  $p < 0.05$ ; \*\*,  $p < 0.01$ ; \*\*\*,  $p < 0.001$ . See also Figure S3 and S4.



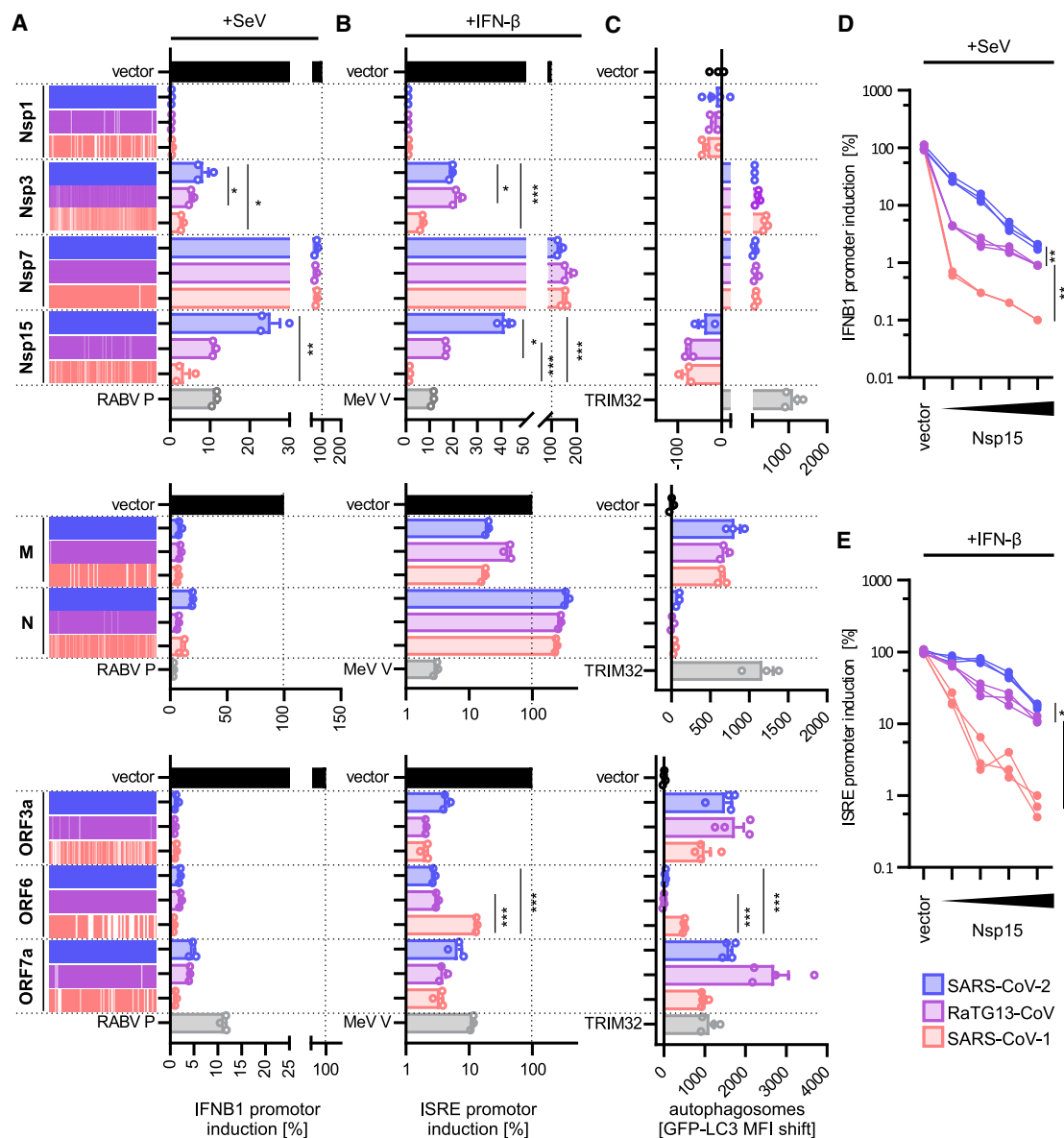


**Figure 5. Functional conservation of innate immune antagonism between SARS-CoV-2, RaTG13-CoV, and SARS-CoV-1**

(A–C) Immune activation of type I IFN induction (A), type I IFN signaling (B), or autophagy (C) in the presence of indicated proteins (Nsp1, Nsp3, Nsp7, Nsp15, M, N, ORF3a, ORF6, and ORF7a) of SARS-CoV-2 (blue), RaTG13-CoV (purple), or SARS-CoV-1 (red) assessed by IFN- $\beta$ -promotor luciferase reporter gene assays stimulated with Sendai virus (SeV; A). ISRE-promotor luciferase reporter gene assays stimulated with IFN- $\beta$  (1,000 U/mL; B) or membrane-associated GFP-LC3B (C). Vector induction set to 100% (black). Controls are Rabies virus P, Measles virus V, or TRIM32 (gray). Bars represent the mean of  $n = 3 \pm$  SEM (biological replicates) (A and B) or  $n = 4 \pm$  SEM (biological replicates) (C).

(D) Dose dependent effect of SARS-CoV-2, RaTG13-CoV or SARS-CoV-1 Nsp15 expression in HEK293T cells on IFN- $\beta$  induction stimulated with SeV (24 h). Quantification by IFN- $\beta$  promotor dependent luciferase reporter activity. Lines represent one individual replicate.

(E) Dose-dependent effect of Nsp15 expression on IFN- $\beta$  signaling in HEK293T cells, stimulated with IFN- $\beta$  (1,000 U/mL, 8 h). Quantification by ISRE-promotor-dependent luciferase reporter activity. Lines represent one individual replicate.

\*,  $p < 0.05$ ; \*\*,  $p < 0.01$ ; \*\*\*,  $p < 0.001$ . See also Figure S5.

caused little if any cytotoxic effects (Figure S6C). The average remaining pathway activity of IFN- $\gamma$  and IFN- $\lambda$ 1 signaling in the presence of SARS-CoV-2 proteins was 82% and 89%, respectively, compared to type I IFN signaling, with a remaining pathway activity of 22% for IFN- $\alpha$ 2 and 47% for IFN- $\beta$  (Fig-

ure 1C). We found a significant inverse correlation ( $r = 0.89$ ) between the average remaining activity of the respective signaling pathway in the presence of all SARS-CoV-2 proteins tested (Figure 1C) and IFN susceptibility at 5 U/mL (Figure 6C). Autophagic turnover was strongly repressed by at least four SARS-CoV-2

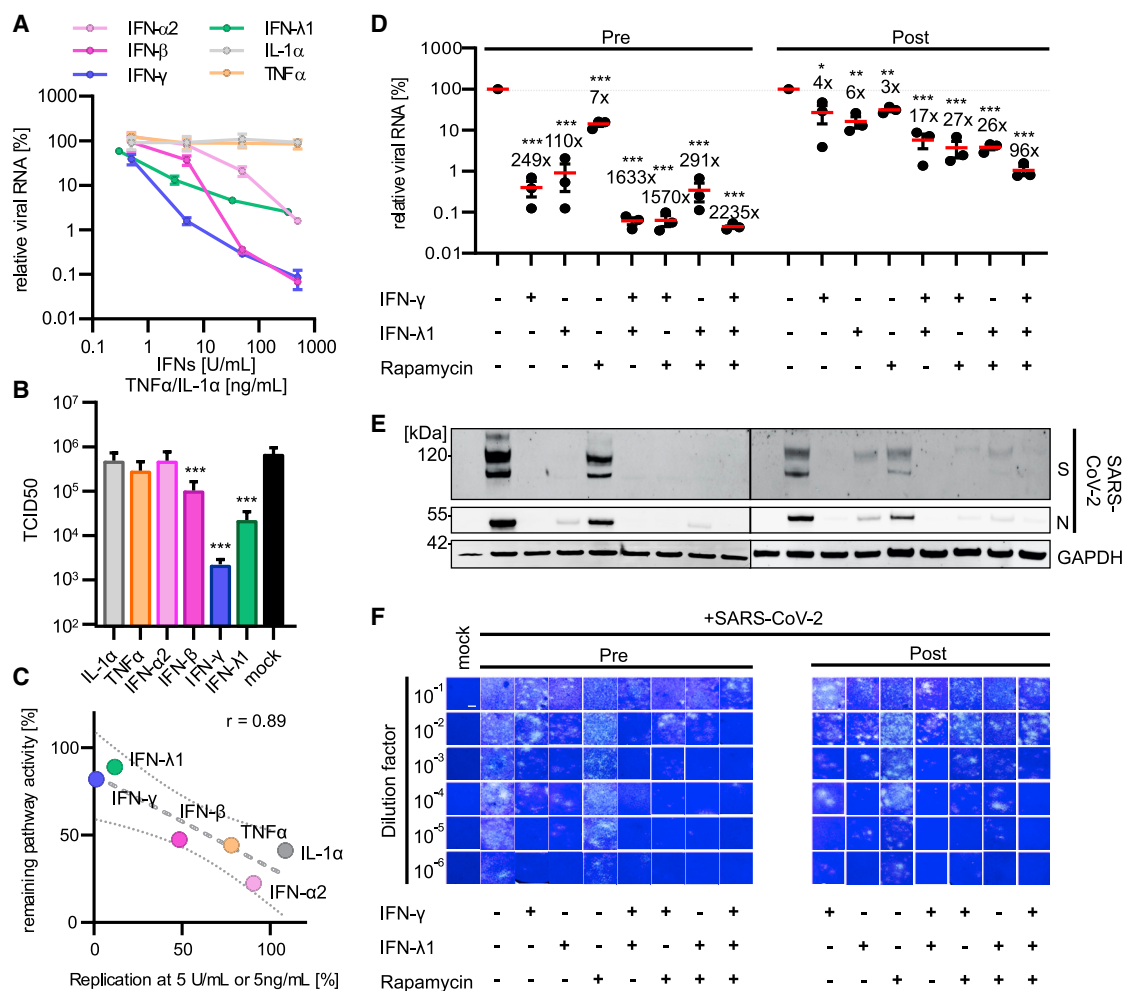


**Figure 6. Concerted innate immune activation as an anti-viral approach**

(A) Quantification of SARS-CoV-2 N RNA in the supernatant of SARS-CoV-2-infected (MOI, 0.05; 48 h post infection [p.i.]) Calu-3 cells that were left untreated and/or were treated with indicated IFNs or pro-inflammatory cytokines as assessed by qPCR. Lines represent the mean of  $n = 2 \pm$  SD (technical replicates).

(B) TCID<sub>50</sub> measurements of the assay in (A), at 5 IU/mL or 5 ng/mL of indicated compounds. Bars represent the mean of  $n = 3 \pm$  SEM (biological replicates).

(C) Correlation between average inhibition of the indicated innate immune signaling pathway and impact on replication of SARS-CoV-2 after treatment with the respective cytokine.  $r$ , Pearson's correlation.

(D) Quantification of SARS-CoV-2 N RNA in the supernatant of SARS-CoV-2-infected (MOI, 0.05; 48 h p.i.) Calu-3 cells that were left untreated and/or were treated with the indicated combinations of IFN-γ or IFN-λ1 (5 U/mL) or rapamycin (125 nM) either 24 h before the infection (pre) or 6 h post-infection (post). Dots represent individual experiments, and the lines represent the mean of  $n = 3 \pm$  SEM (biological replicates). Fold reduction compared to control is indicated.

(E) Exemplary immunoblot analysis of the SARS-CoV-2 infection by using WCLs of Calu-3 cells in (D). Blots were stained with anti-SARS-CoV-2 S, anti-SARS-CoV-2 N, and anti-GAPDH.

(F) Exemplary images of cytopathic effect on Vero cells induced by infectious SARS-CoV-2 containing supernatant (SN) from (D), 48 h post-infection with indicated serial dilutions. Living cells were stained with crystal violet. Scale bar, 5 mm.

\*,  $p < 0.05$ ; \*\*,  $p < 0.01$ ; \*\*\*,  $p < 0.001$ . See also Figure S6.

proteins (Figures 1D and 3B). Thus, we would expect that modulation of autophagy only weakly affects SARS-CoV-2 replication. Indeed, treatment with rapamycin, which induces autophagy, reduced viral replication moderately to a maximum of 4- to 6-fold (Figures S6D and S6E). Bafilomycin A1, which blocks autophagy, had little if any effects (Figure S6E). Both drugs were used at non-toxic concentrations (Figure S6F).

In conclusion, our results indicate that the overall efficiency of SARS-CoV-2 proteins in counteracting specific signaling

pathways correlates with the overall anti-viral potency of the types of IFNs.

### Rational innate immune activation allows highly effective control of SARS-CoV-2

To minimize detrimental pro-inflammatory effects of IFNs in therapeutic approaches, doses required for efficient viral restriction need to be reduced. Thus, we analyzed the impact of the most potent IFNs, IFN-γ, and IFN-λ1 and combinations thereof on

SARS-CoV-2 replication in Calu-3 cells. To mimic prophylactic and therapeutic settings, we examined pre-treatment for 24 h before infection with SARS-CoV-2 and treatment 6 h post-infection. Overall, the effects of IFN treatment were more than 10-fold stronger in the prophylactic condition than in the therapeutic treatment (Figures 6D–6F, S6G, and S6H). Pre-treatment with a single dose of IFN- $\gamma$  or IFN- $\lambda$ 1 reduced viral RNA production by 100- to 250-fold, and the combinatorial treatment achieved a synergistic  $\sim$ 1,600-fold reduction in SARS-CoV-2 RNA released by infected cells (Figure 6D). Post-infection treatment with either IFN- $\gamma$  or IFN- $\lambda$ 1 reduced viral RNA in the supernatant by 4- to 6-fold, and combination of both cytokines reduced SARS-CoV-2 RNA  $\sim$ 17-fold (Figure 6D). Expression analysis of SARS-CoV-2 S and N by western blotting confirmed the qPCR results, and equal GAPDH levels exclude effects on viral replication by cytotoxicity (Figure 6E). A strategy to further decrease inflammatory side effects of IFN treatment is induction of anti-inflammatory pathways like autophagy (Deretic et al., 2013; Levine et al., 2011; Matsuzawa-Ishimoto et al., 2018). Treatment with rapamycin alone already reduced viral replication  $\sim$ 3- to 7-fold at 125 nM (Figure 6D). Treatment of rapamycin (125 nM) in combination with either IFN- $\gamma$  or IFN- $\lambda$ 1 had additive effects (Figures 6D–6F). Triple treatment with IFN- $\gamma$ , IFN- $\lambda$ 1, and rapamycin showed the most potent anti-viral effect for pre- and post-infection treatment, reducing viral RNA in the supernatant by 2,235-fold and 96-fold, respectively (Figure 6D). Quantification of the infectious viral particles released after treatment with the drugs or cytokines showed an even more pronounced effect on viral replication than the qPCR data indicated (Figures 6F and S6I). For instance, triple treatment of rapamycin, IFN- $\lambda$ 1, and IFN- $\gamma$  reduced viral cytopathic effect and plaques more than 10,000- and 1,000-fold, respectively, for pre- and post-infection treatment conditions (Figures 6F and S6I).

In summary, combinatorial treatments with IFN- $\gamma$  and IFN- $\lambda$ 1 are synergistic, and additional activation of anti-inflammatory autophagy by rapamycin further decreased SARS-CoV-2 replication.

## DISCUSSION

Viruses drastically alter human innate immune defenses to establish an infection and propagate to the next host (Chiang et al., 2018; Choi et al., 2018; Frieman et al., 2008; Lei et al., 2020; Stukalov et al., 2020; Takeuchi and Akira, 2009). Our data reveal the extent of immune manipulation used by SARS-CoV-2. We determined the major antagonists of type I IFN induction and type I, II, and III signaling as well as pro-inflammatory NF- $\kappa$ B activity encoded by SARS-CoV-2 (Nsp1, Nsp5, Nsp13, Nsp14, ORF6, and ORF7b). Autophagy is majorly targeted by Nsp15, ORF3a, E, M, and ORF7a. Subsequent mechanistic studies revealed that SARS-CoV-2 proteins synergistically block type I IFN signaling and autophagy at various levels. We reveal that Nsp14 expression induced degradation of the type I IFN receptor IFNAR1, thus blocking activation of the crucial transcription factors STAT1 and STAT2. Both ORF3a and ORF7a stopped autophagic degradation but use two different mechanisms as follows: ORF3a prevented autophagosome-lysosome fusion, and ORF7a reduced the acidity of fused autophagolysosomes. The mechanism of

ORF3a was confirmed in a recent report (Miao et al., 2021). Examination of the functional conservation showed that SARS-CoV-2 Nsp15 was less efficient in blocking innate immune activation, namely, both type I IFN induction and signaling, than SARS-CoV-1 Nsp15. This may ultimately cause SARS-CoV-2 to be better controlled by the innate immune system than SARS-CoV-1, which might explain the higher numbers of subclinical infections and thus overall lower mortality rates of the current pandemic CoV. Calculation of the remaining pathway activity of IFN/pro-inflammatory cytokine signaling cascades in the presence of SARS-CoV-2 proteins revealed that type I IFN induction and signaling are strongly antagonized by SARS-CoV-2 (Figures 1C and 6C). Consequently, the virus is relatively resistant against type I IFN. However, type II and III IFN signaling are overall seemingly less antagonized. In line with this finding, treatment with IFN- $\gamma$  and IFN- $\lambda$ 1 drastically reduced SARS-CoV-2 replication. Notably, combinatorial treatment of SARS-CoV-2 with these two IFNs was synergistic. Additional induction of anti-inflammatory autophagy further enhanced the anti-viral effect. This may pave the way for future anti-viral therapies against SARS-CoV-2 based on concerted innate immune activation.

Besides the accessory genes, which classically encode immune antagonists, a surprising number of non-structural proteins manipulate innate immunity like Nsp1, which targets cellular translation (Thoms et al., 2020). Many non-structural proteins of CoVs have enzymatic functions, as follows: Nsp3 is a de-ISG/ubiquitinase and protease (Báez-Santos et al., 2014; Lei et al., 2018; Shin et al., 2020), Nsp5 acts as a protease (Muramatsu et al., 2016; Stobart et al., 2013), Nsp13 is an NTPase/Helicase (Ivanov and Ziebuhr, 2004; Shu et al., 2020), and Nsp15 is an endoribonuclease (Deng and Baker, 2018). It is known that the de-ISGase activity of Nsp3 is required to inactivate the transcription factor IRF3 and immune sensor MDA5 and thus reduce IFN induction (Liu et al., 2020; Shin et al., 2020). This suggests that the enzymatic function of other Nsps and their role in innate immune evasion may be linked and thus could represent a target for therapy.

Why would multiple effective proteins target the same pathway? Our assays revealed that the targeting mechanisms are not redundant and may act synergistically (Figures 1, 2, 3, and 4). This could allow the virus to tightly control the targeted pathway, thus minimizing the anti-viral effect of innate immune activation. Notably, several proteins of SARS-CoV-2 involved in immune evasion including ORF6, ORF3a, ORF7a, M, and E accumulate at the Golgi network or in perinuclear spaces, alluding to the emerging role of the Golgi as a hub for immune manipulation (Kagan, 2012; Tao et al., 2020). Future studies will hopefully see more mechanistic data on SARS-CoV-2 proteins and unravel their combined role during the infection.

Although our screening approach may pick up most counteraction strategies, we possibly miss some. For example, many non-structural proteins form complexes, which are not present upon individual overexpression. Expression levels of the viral proteins during an infection may impact the strength of the antagonism, which will not be reflected by their individual overexpression. In addition, tagging the proteins may alter their function. Finally, the virus itself may hide from recognition, not activating innate immune defenses in the first place.

Several factors responsible in viral innate immune antagonism appeared to be largely conserved in the SARS-CoV-2 closest related bat isolate RaTG13-CoV (Figure 5). This suggests that the bat virus is capable of counteracting the human immune defenses, which may have facilitated successful zoonotic transmission from bat to humans. Our data show that SARS-CoV-2 Nsp15 is less efficient in IFN evasion than Nsp15 of SARS-CoV-1. Infection with SARS-CoV-2 is often asymptomatic and controlled by the host (Lokugamage et al., 2020), as suggested by the lower mortality rates and higher subclinical infections (Huang et al., 2020) than the previous epidemic SARS-CoV-1. Thus, SARS-CoV-2 may have found the “perfect” balance. Leaky immune evasion and thus intermediate pathogenicity do not kill the host. Paradoxically, this may have supported the fast spread of the virus. It is tempting to speculate that common cold CoVs counteract the innate immune system even less efficiently than SARS-CoV-2.

Severe side effects are prevalent during IFN therapy (Fried, 2002; Neri et al., 2010; van Zonneveld et al., 2005). However, the side effects are dose dependent (Sleijfer et al., 2005). Thus, minimizing the dose by using the most effective IFN is paramount. We show that type II and type III IFNs were most active against SARS-CoV-2 at low concentrations (Figure 6). This finding is supported by recent reports (Busnadiego et al., 2020; Nchioua et al., 2020; Stanifer et al., 2020). One possible explanation would be that there was evolutionarily no need for the virus to antagonize, e.g., type II IFN signaling. Indeed, in COVID-19 patients and *in vitro* infections with SARS-CoV-2, IFN- $\gamma$  levels are surprisingly low (Blanco-Melo et al., 2020; Hadjadj et al., 2020). Furthermore, the SARS-CoV-2 cytokine storm has low IFN- $\gamma$  levels, and decreased IFN- $\gamma$  expression in CD4+ T cells is associated with severe COVID-19 (Chen et al., 2020; Huang et al., 2020; Tay et al., 2020). It is tempting to speculate that T cells that confer pre-existing immunity against SARS-CoV-2 (Le Bert et al., 2020; Sette and Crotty, 2020) could, upon activation, release IFN- $\gamma$ , whose innate immune signaling may also contribute to clearance of the infection. Our data further indicate that treatment with multiple IFNs is synergistic (Figure 6). Thus, a promising antiviral approach may be a combinatorial treatment with different types of cytokines, effectively also reducing the burden of side effects. Combined with anti-inflammatory approaches such as autophagy activation by rapamycin (Deretic et al., 2013; Matsuzawa-Ishimoto et al., 2018), this approach may even be more successful, as our *in vitro* data suggest. Future studies and clinical trials are highly warranted to study rational, concerted innate immune activation against SARS-CoV-2 *in vivo*.

In summary, our results reveal the extent of innate immune manipulation of SARS-CoV-2 and the molecular mechanisms of Nsp14, ORF3a, and ORF7a. A functional comparison to SARS-CoV-1 revealed that mutations in Nsp15 may be responsible for the higher susceptibility of SARS-CoV-2 against IFNs. Finally, our data allowed us to deduce the combinatorial application of IFN- $\gamma$  and IFN- $\lambda$ 1 as a potent immune activation strategy against SARS-CoV-2.

## STAR★METHODS

Detailed methods are provided in the online version of this paper and include the following:

- **KEY RESOURCES TABLE**
- **RESOURCE AVAILABILITY**
  - Lead contact
  - Materials availability
  - Data and code availability
- **EXPERIMENTAL MODEL AND SUBJECT DETAILS**
  - Cell lines
- **METHOD DETAILS**
  - Cloning of expression constructs
  - Transfections
  - Luciferase assays
  - Cell viability assay
  - Autophagy quantification by flow cytometry
  - Whole-cell lysates
  - SDS-PAGE and immunoblotting
  - Immunofluorescence
  - Autophagy quantification by counting
  - Quantification of autophagosome acidification by flow cytometry
  - Quantification of acidic organelles by flow cytometry
  - Quantification of total and acidified autophagosomes by counting
  - RT-qPCR
  - Legendplex ELISA
  - Inhibition of SARS-CoV-2 by immune modulation
  - Propagation of SARS-CoV-2
  - Proteome analysis
  - GO Analysis
  - Half-life analysis
- **QUANTIFICATION AND STATISTICAL ANALYSIS**

## SUPPLEMENTAL INFORMATION

Supplemental information can be found online at <https://doi.org/10.1016/j.celrep.2021.109126>.

## ACKNOWLEDGMENTS

We thank Regina Burger, Susanne Engelhart, Jana-Romana Fischer, Daniela Krnavek, Kerstin Regensburger, Martha Meyer, Birgit Ott, and Nicola Schrott for excellent technical assistance. We would like to acknowledge the library of SARS-CoV-2 expression plasmids that was generously given to us by Nevan Krogan (University of California, San Francisco). Additionally, we thank Dorota Kmiec (Kings College, London) for critical comments and discussion. M.H.C. was funded by an Argelander grant of the University of Bonn. L.K. is supported by a Baustein grant from Ulm University. This study was supported by the German Research Foundation (DFG) grants to F.K. (CRC1279 and SPP1923), J.M. (CRC1279), J.A.M. (MU4485/1-1), K.M.J.S. (CRC1279, SPP1923, SP1600/4-1, and SP1600/6-1), D. Sauter (SPP1923, Heisenberg Programme), F.I.S. (SPP1923), A.I. (CRC1309), and K.-K.C. (TRR237); EU's Horizon 2020 research and innovation program to J.M. (Fight-nCoV, 101003555); COVID-19 research grants of the State Ministry of Baden-Württemberg for Sciences, Research and Arts (to D.S. and F.K.); and the Federal Ministry for Education and Research (BMBF) to F.K. (Restrict SARS-CoV-2), D.S. (protACT), and K.M.J.S. (IMMUNOMOD).

## AUTHOR CONTRIBUTIONS

L.K., M. Hirschenberger, and M. Hayn performed the majority of the experimental work with help from J.H.S., S.K., C.P.B., and V.H. R.N. and F.Z. worked with infectious SARS-CoV-2. D.S. contributed NF- $\kappa$ B reporter experiments and performed additional experimental work. C.M.S. and S.S.B. generated



expression constructs. J.A.M., C.C., and J.M. performed the SARS-CoV-2 infection for the proteome analysis. F.I.S. and M.H.C. provided additional reagents, analyses, and comments. A.I., I.F., and W.A. performed the proteome analyses and the bioinformatic interrogation of the data. J.M., D.S., A.I., S.S.B., and K.-K.C. provided resources and comments for the manuscript. K.M.J.S. and F.K. conceived the study, planned experiments, and wrote the manuscript. All authors reviewed and approved the manuscript.

## DECLARATION OF INTERESTS

F.I.S. is a co-founder of DiosCURE Therapeutics SE and a consultant to IFM Therapeutics.

Received: November 10, 2020

Revised: March 3, 2021

Accepted: April 22, 2021

Published: May 18, 2021

## REFERENCES

- Andersen, K.G., Rambaut, A., Lipkin, W.I., Holmes, E.C., and Garry, R.F. (2020). The proximal origin of SARS-CoV-2. *Nat. Med.* 26, 450–452.
- Báez-Santos, Y.M., Mielech, A.M., Deng, X., Baker, S., and Mesecar, A.D. (2014). Catalytic function and substrate specificity of the papain-like protease domain of nsp3 from the Middle East respiratory syndrome coronavirus. *J. Virol.* 88, 12511–12527.
- Bastard, P., Rosen, L.B., Zhang, Q., Michailidis, E., Hoffmann, H.-H., Zhang, Y., Dorgham, K., Philippot, Q., Rosain, J., Béziat, V., et al.; HGID Lab; NIAID-USUHS Immune Response to COVID Group; COVID Clinicians; COVID-STORM Clinicians; Imagine COVID Group; French COVID Cohort Study Group; Milieu Intérieur Consortium; CoV-Contact Cohort; Amsterdam UMC Covid-19 Biobank; COVID Human Genetic Effort (2020). Autoantibodies against type I IFNs in patients with life-threatening COVID-19. *Science* 370, 80.
- Blanco-Melo, D., Nilsson-Payant, B.E., Liu, W.C., Uhl, S., Hoagland, D., Möller, R., Jordan, T.X., Oishi, K., Panis, M., Sachs, D., et al. (2020). Imbalanced Host Response to SARS-CoV-2 Drives Development of COVID-19. *Cell* 181, 1036–1045.e9.
- Bozzo, C.P., Nchioua, R., Volcic, M., Wettstein, L., Weil, T., Krüger, J., Heller, S., Conzelmann, C., Müller, J., Gross, R., et al. (2020). IFITM proteins promote SARS-CoV-2 infection of human lung cells. *bioRxiv*. <https://doi.org/10.1101/2020.08.18.255935>.
- Brandizzi, F., and Barlowe, C. (2013). Organization of the ER-Golgi interface for membrane traffic control. *Nat. Rev. Mol. Cell Biol.* 14, 382–392.
- Brzózka, K., Finke, S., and Conzelmann, K.-K. (2005). Identification of the Rabies Virus Alpha/Beta Interferon Antagonist: Phosphoprotein P Interferes with Phosphorylation of Interferon Regulatory Factor 3. *J. Virol.* 79, 7673–7681.
- Busnadiego, I., Fernbach, S., Pohl, M.O., Karakus, U., Huber, M., Trkola, A., Stertz, S., and Hale, B.G. (2020). Antiviral activity of type I, II, and III interferons counterbalances ACE2 inducibility and restricts SARS-CoV-2. *mBio*. 11, e01928, 20.
- Chan-Yeung, M., and Xu, R.-H. (2003). SARS: epidemiology. *Respirology* 8, S9–S14.
- Chen, G., Wu, D., Guo, W., Cao, Y., Huang, D., Wang, H., Wang, T., Zhang, X., Chen, H., Yu, H., et al. (2020). Clinical and immunological features of severe and moderate coronavirus disease 2019. *J. Clin. Invest.* 130, 2620–2629.
- Chiang, J.J., Sparrer, K.M.J., van Gent, M., Lässig, C., Huang, T., Osterrieder, N., Hopfner, K.P., and Gack, M.U. (2018). Viral unmasking of cellular 5S rRNA pseudogene transcripts induces RIG-I-mediated immunity. *Nat. Immunol.* 19, 53–62.
- Choi, Y., Bowman, J.W., and Jung, J.U. (2018). Autophagy during viral infection - a double-edged sword. *Nat. Rev. Microbiol.* 16, 341–354.
- Choudhury, A., Dominguez, M., Puri, V., Sharma, D.K., Narita, K., Wheatley, C.L., Marks, D.L., and Pagano, R.E. (2002). Rab proteins mediate Golgi transport of caveola-internalized glycosphingolipids and correct lipid trafficking in Niemann-Pick C cells. *J. Clin. Invest.* 109, 1541–1550.
- Corman, V.M., Muth, D., Niemeyer, D., and Drosten, C. (2018). Hosts and Sources of Endemic Human Coronaviruses. *Adv. Virus Res.* 100, 163–188.
- Deng, X., and Baker, S.C. (2018). An “Old” protein with a new story: Coronavirus endoribonuclease is important for evading host antiviral defenses. *Virology* 517, 157–163.
- Deretic, V., Saitoh, T., and Akira, S. (2013). Autophagy in infection, inflammation and immunity. *Nat. Rev. Immunol.* 13, 722–737.
- Ferretti, L., Wymant, C., Kendall, M., Zhao, L., Nurtay, A., Abeler-Dörner, L., Parker, M., Bonsall, D., and Fraser, C. (2020). Quantifying SARS-CoV-2 transmission suggests epidemic control with digital contact tracing. *Science* 368, eabb6936.
- Fragkou, P.C., Belhadi, D., Peiffer-Smadja, N., Moschopoulos, C.D., Lescure, F.X., Janocha, H., Karofylakis, E., Yazdanpanah, Y., Mentré, F., Skevaki, C., et al. (2020). Review of trials currently testing treatment and prevention of COVID-19. *Clin. Microbiol. Infect.* 26, 988–998.
- Fried, M.W. (2002). Side effects of therapy of hepatitis C and their management. *Hepatology* 36, S237–S244.
- Frieman, M., Heise, M., and Baric, R. (2008). SARS coronavirus and innate immunity. *Virus Res.* 133, 101–112.
- Gordon, D.E., Jang, G.M., Bouhaddou, M., Xu, J., Obernier, K., White, K.M., O’Meara, M.J., Rezelj, V.V., Guo, J.Z., Swaney, D.L., et al. (2020). A SARS-CoV-2 protein interaction map reveals targets for drug repurposing. *Nature* 583, 459–468.
- Hachim, A., Kavian, N., Cohen, C.A., Chin, A.W.H., Chu, D.K.W., Mok, C.K.P., Tsang, O.T.Y., Yeung, Y.C., Perera, R.A.P.M., Poon, L.L.M., et al. (2020). ORF8 and ORF3b antibodies are accurate serological markers of early and late SARS-CoV-2 infection. *Nat. Immunol.* 21, 1293–1301.
- Hadjadj, J., Yatim, N., Barnabei, L., Comeau, A., Boussier, J., Smith, N., Péré, H., Charbit, B., Bondet, V., Chenevier-Gobeaux, C., et al. (2020). Impaired type I interferon activity and inflammatory responses in severe COVID-19 patients. *Science* 369, 718–724.
- Hansen, M.D., Johnsen, I.B., Stiberg, K.A., Sherstova, T., Wakita, T., Richard, G.M., Kandasamy, R.K., Meurs, E.F., and Anthonson, M.W. (2017). Hepatitis C virus triggers Golgi fragmentation and autophagy through the immunity-related GTPase M. *Proc. Natl. Acad. Sci. U S A* 114, E3462–E3471.
- Huang, C., Wang, Y., Li, X., Ren, L., Zhao, J., Hu, Y., Zhang, L., Fan, G., Xu, J., Gu, X., et al. (2020). Clinical features of patients infected with 2019 novel coronavirus in Wuhan. *Lancet* 395, 497–506.
- Hung, I.F.N., Lung, K.C., Tso, E.Y.K., Liu, R., Chung, T.W.H., Chu, M.Y., Ng, Y.Y., Lo, J., Chan, J., Tam, A.R., et al. (2020). Triple combination of interferon beta-1b, lopinavir-ritonavir, and ribavirin in the treatment of patients admitted to hospital with COVID-19: an open-label, randomised, phase 2 trial. *Lancet* 395, 1695–1704.
- Ivanov, K.A., and Ziebuhr, J. (2004). Human Coronavirus 229E Nonstructural Protein 13: Characterization of Duplex-Unwinding, Nucleoside Triphosphatase, and RNA 5′-Triphosphatase Activities. *J. Virol.* 78, 7833–7838.
- Iwasaki, A., and Medzhitov, R. (2010). Regulation of adaptive immunity by the innate immune system. *Science* 327, 291–295.
- Iwasaki, A., and Medzhitov, R. (2015). Control of adaptive immunity by the innate immune system. *Nat. Immunol.* 16, 343–353.
- Kagan, J.C. (2012). Signaling organelles of the innate immune system. *Cell* 151, 1168–1178.
- Kell, A.M., and Gale, M., Jr. (2015). RIG-I in RNA virus recognition. *Virology* 479–480, 110–121.
- Kimura, I., Konno, Y., Sauter, D., Nakagawa, S., and Sato, K. (2021). Sarbecovirus ORF6 Proteins Hamper the Induction of Interferon Signaling by Blocking mRNA Nuclear Export. *Cell Rep.* 34, 108916.
- Klionsky, D.J., Abdelmohsen, K., Abe, A., Abedin, M.J., Abeliovich, H., Arozana, A.A., Adachi, H., Adams, C.M., Adams, P.D., Adeli, K., et al. (2016).

Guidelines for the use and interpretation of assays for monitoring autophagy (3rd edition). *Autophagy* 12, 1–222.

Koepeke, L., Winter, B., Grenzner, A., Regensburger, K., Engelhart, S., van der Merwe, J.A., Krebs, S., Blum, H., Kirchhoff, F., and Sparrer, K.M.J. (2020). An improved method for high-throughput quantification of autophagy in mammalian cells. *Sci. Rep.* 10, 12241.

Koepeke, L., Gack, M.U., and Sparrer, K.M. (2021). The antiviral activities of TRIM proteins. *Curr. Opin. Microbiol.* 59, 50–57.

Konno, Y., Kimura, I., Uriu, K., Fukushi, M., Irie, T., Koyanagi, Y., Sauter, D., Gifford, R.J., Nakagawa, S., and Sato, K. (2020). SARS-CoV-2 ORF3b is a potent interferon antagonist whose activity is further increased by a naturally occurring elongation variant. *bioRxiv*. <https://doi.org/10.1101/2020.05.11.088179>.

Le Bert, N., Tan, A.T., Kunasegaran, K., Tham, C.Y.L., Hafezi, M., Chia, A., Chng, M.H.Y., Lin, M., Tan, N., Linster, M., et al. (2020). SARS-CoV-2-specific T cell immunity in cases of COVID-19 and SARS, and uninfected controls. *Nature* 584, 457–462.

Lei, J., Kusov, Y., and Hilgenfeld, R. (2018). Nsp3 of coronaviruses: Structures and functions of a large multi-domain protein. *Antiviral Res.* 149, 58–74.

Lei, X., Dong, X., Ma, R., Wang, W., Xiao, X., Tian, Z., Wang, C., Wang, Y., Li, L., Ren, L., et al. (2020). Activation and evasion of type I interferon responses by SARS-CoV-2. *Nat. Commun.* 11, 3810.

Levine, B., Mizushima, N., and Virgin, H.W. (2011). Autophagy in immunity and inflammation. *Nature* 469, 323–335.

Liu, G.Q., Lee, J.H., Parker, Z.M., Acharya, D., Chiang, J.J., van Gent, M., Riedl, W., Davis-Gardner, M.E., Wies, E., Chiang, C., et al. (2020). ISG15-dependent Activation of the RNA Sensor MDA5 and its Antagonism by the SARS-CoV-2 papain-like protease. *bioRxiv*. <https://doi.org/10.1101/2020.10.26.356048>.

Lokugamage, K., Hage, A., de Vries, M., Valero-Jimenez, A., Schindewolf, C., Dittmann, M., Rajsbaum, R., and Menachery, V. (2020). Type I interferon susceptibility distinguishes SARS-CoV-2 from SARS-CoV. *bioRxiv*. <https://doi.org/10.1101/2020.03.07.982264>.

Mathieson, T., Franken, H., Kosinski, J., Kurazawa, N., Zinn, N., Sweetman, G., Poeckel, D., Ratnu, V.S., Schramm, M., Becher, I., et al. (2018). Systematic analysis of protein turnover in primary cells. *Nat. Commun.* 9, 689.

Matsuzawa-Ishimoto, Y., Hwang, S., and Cadwell, K. (2018). Autophagy and Inflammation. *Annu. Rev. Immunol.* 36, 73–101.

Miao, G., Zhao, H., Li, Y., Ji, M., Chen, Y., Shi, Y., Bi, Y., Wang, P., and Zhang, H. (2021). ORF3a of the COVID-19 virus SARS-CoV-2 blocks HOPS complex-mediated assembly of the SNARE complex required for autolysosome formation. *Dev. Cell* 56, 427–442.e5.

Muramatsu, T., Takemoto, C., Kim, Y.T., Wang, H., Nishii, W., Terada, T., Shirouzu, M., and Yokoyama, S. (2016). SARS-CoV 3CL protease cleaves its C-terminal autoproteolytic site by novel subsite cooperativity. *Proc. Natl. Acad. Sci. U S A* 113, 12997–13002.

Nchioua, R., Kmiec, D., Mueller, J., Conzelmann, C., Gross, R., Swanson, C.M., Neil, S., Stenger, S., Sauter, D., Muench, J., et al. (2020). The Zinc Finger Antiviral Protein restricts SARS-CoV-2. *bioRxiv*. <https://doi.org/10.1101/2020.06.04.134379>.

Neri, S., Bertino, G., Petralia, A., Giancarlo, C., Rizzotto, A., Calvagno, G.S., Mauceri, B., Abate, G., Boemi, P., Di Pino, A., et al. (2010). A Multidisciplinary Therapeutic Approach for Reducing the Risk of Psychiatric Side Effects in Patients With Chronic Hepatitis C Treated With Pegylated Interferon  $\alpha$  and Ribavirin. *J. Clin. Gastroenterol.* 44, e210, 17.

Petersen, E., Koopmans, M., Go, U., Hamer, D.H., Petrosillo, N., Castelli, F., Storgaard, M., Al Khalili, S., and Simonsen, L. (2020). Comparing SARS-CoV-2 with SARS-CoV and influenza pandemics. *Lancet Infect. Dis.* 20, e238–e244.

Pfaller, C.K., and Conzelmann, K.-K. (2008). Measles Virus V Protein Is a Decoy Substrate for IkappaB Kinase alpha and Prevents Toll-Like Receptor 7/9-Mediated Interferon Induction. *J. Virol.* 82, 12365–12373.

Progida, C., and Bakke, O. (2016). Bidirectional traffic between the Golgi and the endosomes - machineries and regulation. *J. Cell Sci.* 129, 3971–3982.

Sallard, E., Lescure, F.X., Yazdanpanah, Y., Mentre, F., and Peiffer-Smadja, N. (2020). Type 1 interferons as a potential treatment against COVID-19. *Antiviral Res.* 178, 104791.

Schubert, K., Karousis, E.D., Jomaa, A., Scaiola, A., Echeverria, B., Gurseler, L.A., Leibundgut, M., Thiel, V., Mühlemann, O., and Ban, N. (2020). SARS-CoV-2 Nsp1 binds the ribosomal mRNA channel to inhibit translation. *Nat. Struct. Mol. Biol.* 27, 959–966.

Sette, A., and Crotty, S. (2020). Pre-existing immunity to SARS-CoV-2: the knowns and unknowns. *Nat. Rev. Immunol.* 20, 457–458.

Shalhoub, S. (2020). Interferon beta-1b for COVID-19. *Lancet* 395, 1670–1671.

Shin, D., Mukherjee, R., Grewe, D., Bojkova, D., Baek, K., Bhattacharya, A., Schulz, L., Wiedera, M., Mehdipour, A.R., Tascher, G., et al. (2020). Papain-like protease regulates SARS-CoV-2 viral spread and innate immunity. *Nature* 587, 657–662.

Shu, T., Huang, M., Wu, D., Ren, Y., Zhang, X., Han, Y., Mu, J., Wang, R., Qiu, Y., Zhang, D.Y., et al. (2020). SARS-Coronavirus-2 Nsp13 Possesses NTPase and RNA Helicase Activities That Can Be Inhibited by Bismuth Salts. *Virol. Sin.* 35, 321–329.

Sleijfer, S., Bannink, M., Van Gool, A.R., Kruit, W.H.J., and Stoter, G. (2005). Side effects of interferon- $\alpha$  therapy. *Pharm. World Sci.* 27, 423–431.

Sparrer, K.M.J., and Gack, M.U. (2015). Intracellular detection of viral nucleic acids. *Curr. Opin. Microbiol.* 26, 1–9.

Sparrer, K.M.J., and Gack, M.U. (2018). TRIM proteins: New players in virus-induced autophagy. *PLoS Pathog.* 14, e1006787.

Sparrer, K.M.J., Pfaller, C.K., and Conzelmann, K.-K. (2012). Measles Virus C Protein Interferes with Beta Interferon Transcription in the Nucleus. *J. Virol.* 86, 796–805.

Sparrer, K.M.J., Gableske, S., Zurenski, M.A., Parker, Z.M., Full, F., Baumgart, G.J., Kato, J., Pacheco-Rodriguez, G., Liang, C., Pornillos, O., et al. (2017). TRIM23 mediates virus-induced autophagy via activation of TBK1. *Nat. Microbiol.* 2, 1543–1557.

Stanifer, M.L., Kee, C., Cortese, M., Zumarán, C.M., Triana, S., Mukenhirn, M., Krausslich, H.G., Alexandrov, T., Bartenschlager, R., and Boulant, S. (2020). Critical Role of Type III Interferon in Controlling SARS-CoV-2 Infection in Human Intestinal Epithelial Cells. *Cell Rep.* 32, 107863.

Stobart, C.C., Sexton, N.R., Munjal, H., Lu, X., Molland, K.L., Tomar, S., Mescar, A.D., and Denison, M.R. (2013). Chimeric exchange of coronavirus nsp5 proteases (3CLpro) identifies common and divergent regulatory determinants of protease activity. *J. Virol.* 87, 12611–12618.

Stukalov, A., Girault, V., Grass, V., Bergant, V., Karayel, O., Urban, C., Haas, D.A., Huang, Y., Oubraham, L., Wang, A., et al. (2020). Multi-level proteomics reveals host-perturbation strategies of SARS-CoV-2 and SARS-CoV. *bioRxiv*. <https://doi.org/10.1101/2020.06.17.156455>.

Takeuchi, O., and Akira, S. (2009). Innate immunity to virus infection. *Immunol. Rev.* 227, 75–86.

Tao, Y., Yang, Y., Zhou, R., and Gong, T. (2020). Golgi Apparatus: An Emerging Platform for Innate Immunity. *Trends Cell Biol.* 30, 467–477.

Tay, M.Z., Poh, C.M., Rénia, L., MacAry, P.A., and Ng, L.F.P. (2020). The trinity of COVID-19: immunity, inflammation and intervention. *Nat. Rev. Immunol.* 20, 363–374.

Thoms, M., Buschauer, R., Ameisemeier, M., Koepeke, L., Denk, T., Hirschenberger, M., Kratzat, H., Hayn, M., Mackens-Kiani, T., Cheng, J., et al. (2020). Structural basis for translational shutdown and immune evasion by the Nsp1 protein of SARS-CoV-2. *Science* 369, 1249–1255.

Thorlund, K., Dron, L., Park, J., Hsu, G., Forrest, J.I., and Mills, E.J. (2020). A real-time dashboard of clinical trials for COVID-19. *Lancet Digit. Health* 2, e286–e287.

Totura, A.L., and Baric, R.S. (2012). SARS coronavirus pathogenesis: host innate immune responses and viral antagonism of interferon. *Curr. Opin. Virol.* 2, 264–275.

- van Gent, M., Sparrer, K.M.J., and Gack, M.U. (2018). TRIM proteins and their roles in antiviral host defenses. *Annu. Rev. Virol.* 5, 385–405.
- van Zonneveld, M., Flink, H.J., Verhey, E., Senturk, H., Zeuzem, S., Akarca, U.S., Cakaloglu, Y., Simon, C., So, T.M.K., Gerken, G., et al.; HBV 99-01 Study Group (2005). The safety of pegylated interferon alpha-2b in the treatment of chronic hepatitis B: predictive factors for dose reduction and treatment discontinuation. *Aliment. Pharmacol. Ther.* 21, 1163–1171.
- Wang, N., Zhan, Y., Zhu, L., Hou, Z., Liu, F., Song, P., Qiu, F., Wang, X., Zou, X., Wan, D., et al. (2020). Retrospective Multicenter Cohort Study Shows Early Interferon Therapy Is Associated with Favorable Clinical Responses in COVID-19 Patients. *Cell Host Microbe* 28, 455–464.e2.
- WHO (2020). Influenza and COVID-19—similarities and differences (World Health Organization).
- Wu, F., Zhao, S., Yu, B., Chen, Y.M., Wang, W., Song, Z.G., Hu, Y., Tao, Z.W., Tian, J.H., Pei, Y.Y., et al. (2020). A new coronavirus associated with human respiratory disease in China. *Nature* 579, 265–269.
- Xia, C., Vijayan, M., Pritzi, C.J., Fuchs, S.Y., McDermott, A.B., and Hahm, B. (2016). Hemagglutinin of Influenza A Virus Antagonizes Type I Interferon (IFN) Responses by Inducing Degradation of Type I IFN Receptor 1. *J. Virol.* 90, 2403–2417.
- Xia, H., Cao, Z., Xie, X., Zhang, X., Chen, J.Y.-C., Wang, H., Menachery, V.D., Rajsbaum, R., and Shi, P.-Y. (2020). Evasion of Type I Interferon by SARS-CoV-2. *Cell Rep.* 33, 108234.
- Yuen, C.K., Lam, J.Y., Wong, W.M., Mak, L.F., Wang, X., Chu, H., Cai, J.P., Jin, D.Y., To, K.K.W., Chan, J.F.W., et al. (2020). SARS-CoV-2 nsp13, nsp14, nsp15 and orf6 function as potent interferon antagonists. *Emerg. Microbes Infect.* 9, 1418–1428.
- Zhang, Q., Bastard, P., Liu, Z., Le Pen, J., Moncada-Velez, M., Chen, J., Ogishi, M., Sabli, I.K.D., Hodeib, S., Korol, C., et al. (2020). Inborn errors of type I IFN immunity in patients with life-threatening COVID-19. *Science* 370, eabd4570.
- Zhou, P., Yang, X., Wang, X.G., Hu, B., Zhang, L., Zhang, W., Si, H.R., Zhu, Y., Li, B., Huang, C.-L., et al. (2020a). A pneumonia outbreak associated with a new coronavirus of probable bat origin. *Nature* 579, 270–273.
- Zhou, Q., Chen, V., Shannon, C.P., Wei, X.S., Xiang, X., Wang, X., Wang, Z.H., Tebbutt, S.J., Kollmann, T.R., and Fish, E.N. (2020b). Interferon-alpha 2b Treatment for COVID-19. *Front. Immunol.* 40, 578–588.
- Zumla, A., Hui, D.S., and Perlman, S. (2015). Middle East respiratory syndrome. *Lancet* 386, 995–1007.

## STAR★METHODS

### KEY RESOURCES TABLE

REAGENT or RESOURCE	SOURCE	IDENTIFIER
<b>Antibodies</b>		
Donkey anti-Rabbit IgG (H+L) Highly Cross-Adsorbed Secondary Antibody, Alexa Fluor 568 (1:400, IF)	Thermo Scientific	Cat#A10042; RRID:AB_2534017
Donkey anti-Sheep IgG (H+L) Cross-Adsorbed Secondary Antibody, Alexa Fluor 647 (1:400, IF)	Thermo Scientific	Cat#A21448; RRID:AB_2535865
Goat anti-Mouse IgG (H+L) Highly Cross-Adsorbed Secondary Antibody, Alexa Fluor 568 (1:400, IF)	Thermo Scientific	Cat#A21245; RRID:AB_2535813
Goat anti-Rabbit IgG (H+L) Cross-Adsorbed Secondary Antibody, Alexa Fluor 647 (1:400, IF)	Thermo Scientific	Cat#A11004; RRID:AB_2534072
IRDye 800CW Goat anti-Mouse IgG Secondary Antibody (1:20,000, wb)	LI-COR	Cat#926-32210; RRID:AB_621842
IRDye 800CW Goat anti-Rabbit IgG Secondary Antibody (1:20,000, wb)	LI-COR	Cat#926-32211; RRID:AB_621843
IRDye 800CW Goat anti-Rat IgG Secondary Antibody (1:20,000, wb)	LI-COR	Cat#926-32219; RRID:AB_1850025
IRDye® 680RD Donkey anti-Guinea Pig IgG Secondary Antibody (1:20,000, wb)	LI-COR	Cat#926-68077; RRID:AB_10956079
IRDye® 680RD Goat anti-Mouse IgG Secondary Antibody (1:20,000, wb)	LI-COR	Cat#926-68070; RRID:AB_10956588
IRDye® 680RD Goat anti-Rabbit IgG Secondary Antibody (1:20,000, wb)	LI-COR	Cat#926-68071; RRID:AB_10956166
Monoclonal mouse anti-SARS-CoV-2 spike antibody, 1A9 (1:1,000, wb)	Biozol	Cat#GTX632604; RRID:AB_2864418
Monoclonal mouse anti-FLAG-tag antibody, M2 (1:5,000, wb)	Sigma-Aldrich	Cat#F1804; RRID:AB_262044
Monoclonal mouse anti-Anti-Influenza A H1N1 hemagglutinin antibody; C102 (IV.C102) (1:1,000 wb)	abcam	Cat#ab128412; RRID:AB_11142609
Monoclonal mouse anti-LC3 $\alpha$ /β antibody, G-4 (1:200, wb)	Santa Cruz Biotechnology	Cat#sc-398822; RRID:AB_2877091
Monoclonal mouse anti-SARS-CoV/SARS-CoV-2 Nucleocapsid antibody, MM05 (1:1,000, wb)	SinoBiological	Cat#40143-MM05; RRID:AB_2827977
Monoclonal mouse anti-strep II-tag antibody, 517 (1:1,000, wb) (1:200, IF)	Novus Biologicals	Cat#NBP2-43735
Monoclonal mouse anti-β-actin antibody, AC-15 (1:10,000, wb)	Sigma-Aldrich	Cat#A5441; RRID:AB_476744
Monoclonal rabbit anti-IFNAR1 antibody, EP899Y (1:1,000, wb)	abcam	Cat#ab45172; RRID:AB_775764
Monoclonal rabbit anti-pSTAT1 antibody, Y701, 58D6 (1:1,000, wb)	Cell Signaling Technology	Cat#9167S; RRID:AB_561284
Monoclonal rabbit anti-Rab5 antibody, C8B1 (1:1,000, wb)	Cell Signaling Technology	Cat#3547S; RRID:AB_2300649
Monoclonal rabbit anti-ULK1 antibody, D8H5 (1:1,000, wb)	Cell Signaling Technology	Cat#8054S; RRID:AB_11178668

(Continued on next page)



**Continued**

REAGENT or RESOURCE	SOURCE	IDENTIFIER
Monoclonal rabbit anti-V5-tag antibody, D3H8Q (1:1,000, wb)	Cell Signaling Technology	Cat#13202S; RRID:AB_2687461
Monoclonal rat anti-GAPDH antibody, W17079A (1:1,000, wb)	Biolegend	Cat#607902; RRID:AB_2734503
Polyclonal guinea pig anti-p62 antibody, (1:1,000, wb)	ProGen	Cat#GP62-N; RRID:AB_2801426
Polyclonal rabbit anti-Beclin-1 antibody, (1:1,000, wb)	Cell Signaling Technology	Cat#3738S; RRID:AB_490837
Polyclonal rabbit anti-pSTAT2 antibody, Y690 (1:1,000, wb)	Cell Signaling Technology	Cat#4441S; RRID:AB_2198445
Polyclonal rabbit anti-SARS-CoV-2 Nsp3 antibody, (1:1,000, wb)	GeneTex	Cat#GTX135614; RRID:AB_2887505
Polyclonal rabbit anti-STAT1 antibody, (1:1,000, wb)	Cell Signaling Technology	Cat#9172S; RRID:AB_2198300
Polyclonal rabbit anti-STAT2 antibody, (1:1,000, wb)	Cell Signaling Technology	Cat#4594S; RRID:AB_2271323
Polyclonal rabbit anti-strep II-tag antibody, (1:2,000, wb)	abcam	Cat#ab76949; RRID:AB_1524455
Polyclonal sheep anti-TGN46 antibody, (1:400, IF)	Bio Rad	Cat#AHP500GT; RRID:AB_2203291
Monoclonal rabbit anti-LAMP1 antibody, D2D11 (1:200, IF)	Cell Signaling Technologies	Cat#90919; RRID:AB_2687579

**Virus strains**

BetaCoV/France/IDF0372/2020	European Virus Archive	#014V-03890
BetaCoV/Netherlands/01/NL/2020	European Virus Archive	#010V-03903
Sendai Virus Cantell strain	Hans-Georg Koch	N/A

**Chemicals, peptides and recombinant proteins**

1% Casein in PBS	Thermo Scientific	Cat#37528
4% Paraformaldehyde	Santa Cruz Biotechnology	Cat#sc-281692
6x Protein Sample Loading Buffer	LI-COR	Cat#928-40004
Anthrax Protective Antigen, Bacillus anthracis	Sigma-Aldrich	Cat#176908
Bafilomycin A1	Santa Cruz Biotechnology	Cat#sc-201550
CellTiter-Glo Luminescent Cell Viability Assay	Promega	Cat#G7570
Chloroquine	Santa Cruz Biotechnology	Cat#sc-205629
DABCO	Carl Roth	Cat#0718
DAPI (4',6-Diamidino-2-Phenylindole, Dihydrochloride) (1:1,000, IF)	Invitrogen	Cat#D1306
Doxycycline	Sigma-Aldrich	Cat#D3072
Dual-Glo luciferase assay system	Promega	Cat#E2920
Dulbecco's Modified Eagle Medium (DMEM)	GIBCO	Cat#41965039
ethylenediaminetetraacetic acid (EDTA)	Sigma-Aldrich	Cat#E9884
fetal bovine serum (FBS)	GIBCO	Cat#10270106
Glycerol	Sigma-Aldrich	Cat#G5516
HCl	VWR	Cat#20252
HEPES	Sigma-Aldrich	Cat#H3375
IFN- $\alpha$ 2	Sigma-Aldrich	Cat#SRP4594
IFN- $\beta$	Merck	Cat#IF014

(Continued on next page)

**Continued**

REAGENT or RESOURCE	SOURCE	IDENTIFIER
IFN- $\gamma$	Sigma-Aldrich	Cat#I3265
IFN- $\lambda$ 1	R&D Systems	Cat#1598-IL
IL-1 $\alpha$	R&D Systems	Cat#200-LA
Immobilon-FL PVDF membrane	Merck Millipore	Cat#IPVH00010
iST-kit	Preomics	Cat#P.O.00027
L-glutamine	PAN-Biotech	Cat#P04-80100
LEGENDplex Human Anti-Virus Response Panel (13-plex) with V-bottom Plate	BioLedgend	Cat#740390
LysoTracker Deep Red	Invitrogen	Cat#L12492
MG132	Sigma-Aldrich	Cat#M8699
Minimum Essential Medium Eagle (MEM)	Sigma-Aldrich	Cat#M4655
Mlul-HF	New England Biolabs	Cat#R3198
Mowiol 4-88	Carl Roth	Cat#0713
NaCl	Merck	Cat#106404
Non-essential amino acids	Sigma-Aldrich	Cat#M7145
NuPAGE 4-12% Bis-Tris Gels	Invitrogen	Cat#NP0321BOX
Opti-MEM	GIBCO	Cat#31985047
Passive lysis buffer	Promega	Cat#E1941
Penicillin-Streptomycin	PAN-Biotech	Cat#P06-07050
Phosphate-Buffered Saline (PBS)	GIBCO	Cat#14190094
Pierce BCA Protein Assay Kit	Thermo Scientific	Cat#23225
PMA	Sigma-Aldrich	Cat#P1585
Polyethylenimine (PEI)	Sigma-Aldrich	Cat#408727
Quick-RNA Microprep Kit	Zymo Reaserch	Cat#R1051
Protease inhibitor	Sigma-Aldrich	Cat#P2714
Rapamycin	Merck	Cat#553211
Saponin	Sigma-Aldrich	Cat#47036
Sodium pyruvate	Sigma-Aldrich	Cat#S8636
SuperScript III Platinum One-Step qRT-PCR Kit	Thermo Fisher	Cat#11732088
Synthetic SARS-CoV-2-RNA	Twist Bioscience	Cat#102019
TaqMan Fast Virus 1-Step Master Mix	Thermo Fisher	Cat#4444436
TNF $\alpha$	Sigma-Aldrich	Cat#T6674
TransIT-LT1 Transfection Reagent	Mirus	Cat#MIR2300
Tris	AppliChem GmbH	Cat#A2264
Triton X-100	Sigma-Aldrich	Cat#T8787
Trypsin 0.05%/EDTA 0.02%	PAN-Biotech	Cat#P10-023100
Viral RNA Mini Kit	QIAGEN	Cat#52906
Vx-765	InvivoGen	Cat#inh-vx765i-1
XbaI	New England Biolabs	Cat#R0145
$\beta$ -mercaptoethanol	Sigma-Aldrich	Cat#444203

**Experimental models: Cell lines**

African Green Monkey: Vero E6	ATCC	Cat#CRL-1586; RRID:CVCL_0574
Human: Caco-2	Holger Barth	RRID:CVCL_0025
Human: Calu-3	Manfred Frick	RRID:CVCL_0609
Human: HEK293T	ATCC	Cat#CRL3216; RRID:CVCL_0063
Human: HEK293T GL	Konstantin Sparrer	N/A
Human: HEK293T mGL	Konstantin Sparrer	N/A
Human: HeLa GL	Konstantin Sparrer	N/A

(Continued on next page)

**Continued**

REAGENT or RESOURCE	SOURCE	IDENTIFIER
<b>Oligonucleotides</b>		
HKU-N forward: 5'-TAA TCA GAC AAG GAA CTG ATT A-3'	Biomers	N/A
HKU-N probe: 5'-FAM-GCA AAT TGT GCA ATT TGC GG-TAMRA-3'	Biomers	N/A
TaqMan® Gene Expression Assays IFB1 Primer probe	Thermo Fisher	Cat#Hs01077958_s1
TaqMan® Gene Expression Assays IFNAR Primer probe	Thermo Fisher	Cat#Hs01066116_m1
Human GAPD (GAPDH) Endogenous Control (VIC/TAMRA probe)	Thermo Fisher (Applied Biosystems)	Cat#4310884E
HKU-N reverse: 5'-CGA AGG TGT GAC TTC CAT G-3'	Biomers	N/A
<b>Recombinant DNA</b>		
GFP-rab9 WT	Addgene, Richard Pagano	<a href="#">Choudhury et al., 2002</a>
p125-Luc (IFNB1)	Karl-Klaus Conzelmann	<a href="#">Sparrer et al., 2012</a>
p55c1b-Luc (IRF3)	Karl-Klaus Conzelmann	<a href="#">Sparrer et al., 2012</a>
pCG_RaTG-13-M_V5	This paper	N/A
pCG_RaTG-13-N_V5	This paper	N/A
pCG_RaTG-13-Nsp1_V5	This paper	N/A
pCG_RaTG-13-Nsp15_V5	This paper	N/A
pCG_RaTG-13-Nsp3_V5	This paper	N/A
pCG_RaTG-13-Nsp7_V5	This paper	N/A
pCG_RaTG-13-Orf3a_V5	This paper	N/A
pCG_RaTG-13-Orf6_V5	This paper	N/A
pCG_RaTG-13-Orf7a_V5	This paper	N/A
pCG_SARS-CoV-1-M_V5	This paper	N/A
pCG_SARS-CoV-1-N_V5	This paper	N/A
pCG_SARS-CoV-1-Nsp1_V5	This paper	N/A
pCG_SARS-CoV-1-Nsp15_V5	This paper	N/A
pCG_SARS-CoV-1-Nsp3_V5	This paper	N/A
pCG_SARS-CoV-1-Nsp7_V5	This paper	N/A
pCG_SARS-CoV-1-Orf3a_V5	This paper	N/A
pCG_SARS-CoV-1-Orf6_V5	This paper	N/A
pCG_SARS-CoV-1-Orf7a_V5	This paper	N/A
pCG_SARS-CoV-2-M_V5	This paper	N/A
pCG_SARS-CoV-2-N_V5	This paper	N/A
pCG_SARS-CoV-2-Nsp1_V5	This paper	N/A
pCG_SARS-CoV-2-Nsp15_V5	This paper	N/A
pCG_SARS-CoV-2-Nsp3_V5	This paper	N/A
pCG_SARS-CoV-2-Nsp7_V5	This paper	N/A
pCG_SARS-CoV-2-Orf3a_V5	This paper	N/A
pCG_SARS-CoV-2-Orf6_V5	This paper	N/A
pCG_SARS-CoV-2-Orf7a_V5	This paper	N/A
pCR3-Ig-MeV-V	Karl-Klaus Conzelmann	<a href="#">Pfaller and Conzelmann, 2008</a>
pCR3-RV-P	Karl-Klaus Conzelmann	<a href="#">Brzózka et al., 2005</a>
pGAPDH_PROM_01_Renilla SP Luciferase	Switchgear genomics	Cat#S721624
pGAS-Luc	Karl-Klaus Conzelmann	<a href="#">Pfaller and Conzelmann, 2008; Sparrer et al., 2012</a>

(Continued on next page)

**Continued**

REAGENT or RESOURCE	SOURCE	IDENTIFIER
pIFNa4-Luc	Karl-Klaus Conzelmann	Pfaller and Conzelmann, 2008; Sparrer et al., 2012
pIRES_TRIM32_FLAG	Lennart Koepke	Koepke et al., 2020
pISRE-Luc	Karl-Klaus Conzelmann	Pfaller and Conzelmann, 2008; Sparrer et al., 2012
pLVX-EF1alpha-2xStrep-IRES-Puro	David Gordon and Nevan Krogan	Gordon et al., 2020
pLVX-EF1alpha-nCoV2019-E-2xStrep-IRES-Puro	David Gordon and Nevan Krogan	Gordon et al., 2020
pLVX-EF1alpha-nCoV2019-M-2xStrep-IRES-Puro	David Gordon and Nevan Krogan	Gordon et al., 2020
pLVX-EF1alpha-nCoV2019-N-2xStrep-IRES-Puro	David Gordon and Nevan Krogan	Gordon et al., 2020
pLVX-EF1alpha-nCoV2019-Nsp10-2xStrep-IRES-Puro	David Gordon and Nevan Krogan	Gordon et al., 2020
pLVX-EF1alpha-nCoV2019-Nsp11-2xStrep-IRES-Puro	David Gordon and Nevan Krogan	Gordon et al., 2020
pLVX-EF1alpha-nCoV2019-Nsp12-2xStrep-IRES-Puro	David Gordon and Nevan Krogan	Gordon et al., 2020
pLVX-EF1alpha-nCoV2019-Nsp1-2xStrep-IRES-Puro	David Gordon and Nevan Krogan	Gordon et al., 2020
pLVX-EF1alpha-nCoV2019-Nsp13-2xStrep-IRES-Puro	David Gordon and Nevan Krogan	Gordon et al., 2020
pLVX-EF1alpha-nCoV2019-Nsp14-2xStrep-IRES-Puro	David Gordon and Nevan Krogan	Gordon et al., 2020
pLVX-EF1alpha-nCoV2019-Nsp15-2xStrep-IRES-Puro	David Gordon and Nevan Krogan	Gordon et al., 2020
pLVX-EF1alpha-nCoV2019-Nsp16-2xStrep-IRES-Puro	David Gordon and Nevan Krogan	Gordon et al., 2020
pLVX-EF1alpha-nCoV2019-Nsp2-2xStrep-IRES-Puro	David Gordon and Nevan Krogan	Gordon et al., 2020
pLVX-EF1alpha-nCoV2019-Nsp4-2xStrep-IRES-Puro	David Gordon and Nevan Krogan	Gordon et al., 2020
pLVX-EF1alpha-nCoV2019-Nsp5-2xStrep-IRES-Puro	David Gordon and Nevan Krogan	Gordon et al., 2020
pLVX-EF1alpha-nCoV2019-Nsp6-2xStrep-IRES-Puro	David Gordon and Nevan Krogan	Gordon et al., 2020
pLVX-EF1alpha-nCoV2019-Nsp7-2xStrep-IRES-Puro	David Gordon and Nevan Krogan	Gordon et al., 2020
pLVX-EF1alpha-nCoV2019-Nsp8-2xStrep-IRES-Puro	David Gordon and Nevan Krogan	Gordon et al., 2020
pLVX-EF1alpha-nCoV2019-Nsp9-2xStrep-IRES-Puro	David Gordon and Nevan Krogan	Gordon et al., 2020
pLVX-EF1alpha-nCoV2019-Orf10-2xStrep-IRES-Puro	David Gordon and Nevan Krogan	Gordon et al., 2020
pLVX-EF1alpha-nCoV2019-Orf3a-2xStrep-IRES-Puro	David Gordon and Nevan Krogan	Gordon et al., 2020
pLVX-EF1alpha-nCoV2019-Orf3c-2xStrep-IRES-Puro	David Gordon and Nevan Krogan	Gordon et al., 2020
pLVX-EF1alpha-nCoV2019-Orf6-2xStrep-IRES-Puro	David Gordon and Nevan Krogan	Gordon et al., 2020
pLVX-EF1alpha-nCoV2019-Orf7a-2xStrep-IRES-Puro	David Gordon and Nevan Krogan	Gordon et al., 2020
pLVX-EF1alpha-nCoV2019-Orf7b-2xStrep-IRES-Puro	David Gordon and Nevan Krogan	Gordon et al., 2020

(Continued on next page)



**Continued**

REAGENT or RESOURCE	SOURCE	IDENTIFIER
pLVX-EF1alpha-nCoV2019-Orf8-2xStrep-IRES-Puro	David Gordon and Nevan Krogan	<a href="#">Gordon et al., 2020</a>
pLVX-EF1alpha-nCoV2019-Orf9b-2xStrep-IRES-Puro	David Gordon and Nevan Krogan	<a href="#">Gordon et al., 2020</a>
pLVX-EF1alpha-nCoV2019-Orf9c-2xStrep-IRES-Puro	David Gordon and Nevan Krogan	<a href="#">Gordon et al., 2020</a>
pLVX-EF1alpha-nCoV2019-S-2xStrep-IRES-Puro	David Gordon and Nevan Krogan	<a href="#">Gordon et al., 2020</a>
pMD2.G	Addgene, Didier Trono	12259; RRID:Addgene_12259
pNF-kb-Luc	Karl-Klaus Conzelmann	<a href="#">Pfaller and Conzelmann, 2008</a>
psPax2	Addgene, Didier Trono	12260; RRID:Addgene_12260

**Software and algorithms**

Corel DRAW 2017	Corel Corporation	<a href="https://www.coreldraw.com">https://www.coreldraw.com</a>
Fiji (ImageJ) version 1.8	N/A	<a href="https://imagej.net/Fiji">https://imagej.net/Fiji</a>
GraphPad PRISM 8	GraphPad Software, Inc.	<a href="https://www.graphpad.com">https://www.graphpad.com</a>
LI-COR Image Studio Lite Version 5.0	LI-COR	<a href="https://www.licor.com">https://www.licor.com</a>
MATLAB 2019b	MathWorks	<a href="https://www.mathworks.com">https://www.mathworks.com</a>
Biolegend Legendplex v8.0 software	BioLegend	<a href="http://www.biolegend.com">www.biolegend.com</a>
Huygens Professional 19.04 software	Scientific Volume Imaging B.V	<a href="https://www.svi.nl">https://www.svi.nl</a>
R version 4	R Foundation	<a href="http://www.r-project.org">www.r-project.org</a>

**Deposited Data**

Proteomics data	This paper	PRIDE:PXD021899
-----------------	------------	-----------------

**RESOURCE AVAILABILITY**

**Lead contact**

Further information and requests for resources and reagents should be directed to and will be fulfilled by the lead contact, Konstantin Sparrer ([konstantin.sparrer@uni-ulm.de](mailto:konstantin.sparrer@uni-ulm.de)).

**Materials availability**

All unique reagents generated in this study are listed in the [key resources table](#) and available from the lead contact.

**Data and code availability**

Mass spectrometry datasets generated during and/or analyzed during the current study are available in the PRIDE partner repository with the dataset identifier PRIDE: PXD021899. The datasets generated during and/or analyzed during the current study are either included in the study and/or available from the corresponding author on reasonable request.

**EXPERIMENTAL MODEL AND SUBJECT DETAILS**

**Cell lines**

The construction of HEK293T GFP-LC3B(GL) cells and HeLa GL cells was reported previously ([Koepeke et al., 2020](#)). HEK293T, HEK293T GL, HEK293T mGL and HeLa GL cell lines were cultivated in Dulbecco's Modified Eagle Medium (DMEM) supplemented with 10% (v/v) fetal bovine serum (FBS), 100 U/ml penicillin, 100 µg/ml streptomycin, and 2 mM L-glutamine. Calu-3 (human epithelial lung adenocarcinoma, kindly provided and verified by Prof. Frick, Ulm University) cells were cultured in Minimum Essential Medium Eagle supplemented with 10% (v/v) FBS (during viral infection) or 20% (v/v) FBS (during all other times), 100 U/ml penicillin, 100 µg/ml streptomycin, 1 mM sodium pyruvate, and 1x non-essential amino acids. Caco-2 (human epithelial colorectal adenocarcinoma kindly provided by Prof. Barth, Ulm University) cells were maintained in DMEM containing 10% (v/v) FBS, 100 U/ml penicillin, 100 µg/ml streptomycin, 2 mM L-glutamine, 1 mM sodium pyruvate, and 1x non-essential amino acids. Vero E6 (Cercopithecus aethiops derived epithelial kidney cells) cells were maintained in DMEM supplemented with 2.5% (v/v) FBS, 100 U/ml penicillin, 100 µg/ml streptomycin, 2 mM L-glutamine, 1 mM sodium pyruvate, and 1x non-essential amino acids. All cells were cultured at 37°C in a 5% CO<sub>2</sub>, 90% humidity atmosphere.

## METHOD DETAILS

### Cloning of expression constructs

V5 tagged, codon optimized Orfs coding for Nsp1, Nsp3, Nsp7, Nsp15, M, N, Orf3a, Orf6, and Orf7a from SARS-CoV-2, RaTG13, and SARS-CoV-1 were synthesized by Twist Bioscience and subcloned into the pCG vector using restriction cloning with the restriction enzymes XbaI and MluI.

### Transfections

Plasmid DNA was transiently transfected using either the TransIT-LT1 Transfection Reagent or Polyethylenimine (PEI, 1 mg/mL in H<sub>2</sub>O) according to the manufacturers recommendations or as described previously (Bozzo et al., 2020; Koepke et al., 2020).

### Luciferase assays

HEK293T cells were transiently transfected with firefly luciferase reporter constructs, renilla luciferase control constructs, and constructs expressing SARS-CoV-2 Orfs in 48-well plates using TransIT-LT1. One day post-transfection, the cells were stimulated with IFN- $\beta$  (1,000 U/ml, 8 h), IFN- $\alpha$ 2 (500 U/ml, 24 h), IFN- $\gamma$  (400 U/ml, 24 h), IFN- $\lambda$ 1 (100 ng/ml (60 U/mL), 8 h), IL-1 $\alpha$  (10 ng/ml, 24 h), TNF $\alpha$  (25 ng/ml, 24 h), or SeV (1:500, 24 h), 8-24 h post-stimulation/infection, cells were lysed in passive lysis buffer and luciferase activities of the firefly luciferase and renilla luciferase were determined using the Dual-Glo luciferase assay system and an Orion II microplate Luminometer (Berthold). Cell viability of the transfected cells was measured using the CellTiter-Glo Luminescent Cell Viability Assay and an Orion II microplate Luminometer (Berthold).

### Cell viability assay

Calu-3 or HEK293T cells were treated with cytokines or transiently transfected using TransIT-LT1. To measure metabolic activity, cells were lysed in passive lysis buffer and analyzed using the CellTiter-Glo Luminescent Cell Viability Assay according to manufacturer's instructions and an Orion II microplate Luminometer (Berthold).

### Autophagy quantification by flow cytometry

The number of autophagosomes was quantified as previously described (Koepke et al., 2020), either in a basal state, or stimulated with rapamycin (1  $\mu$ M) or Bafilomycin A1 (0.1  $\mu$ M). In brief, HEK293T cells stably expressing GFP-LC3B (HEK293T GL) were transiently transfected using PEI. 48 h post-transfection, cells were harvested in PBS and treated for 20 min at 4°C with PBS containing 0.05% Saponin. Non-membrane bound GFP-LC3B was washed out of the permeabilized cells using PBS twice, followed by fixation in 4% paraformaldehyde. The fluorescence intensity of membrane associated GFP-LC3B was then quantified via flow cytometry (FACS-Canto II, BD Biosciences). The GFP-LC3B mean fluorescence intensity of the control (baseline) was subtracted.

### Whole-cell lysates

Whole-cell lysates were prepared by collecting cells in Phosphate-Buffered Saline (PBS). The cell pellet (500 g, 4°C, 5 min) was lysed in transmembrane lysis buffer [50 mM HEPES pH 7.4, 150 mM NaCl, 1% Triton X-100, 5 mM ethylenediaminetetraacetic acid (EDTA)], supplemented with 1:500 protease inhibitor, by vortexing at maximum speed for 30 s. Cell debris were pelleted by centrifugation (20,000 g, 4°C, 20 min) and the total protein concentration of the cleared lysates was measured using the Pierce BCA Protein Assay Kit according to manufacturer's instructions. The lysates were adjusted to the same protein concentration and stored at -20°C.

### SDS-PAGE and immunoblotting

SDS-PAGE and immunoblotting was performed using standard techniques as previously described (Koepke et al., 2020). In brief, whole cell lysates were mixed with 6x Protein Sample Loading Buffer (at a final dilution of 1x) supplemented with 15%  $\beta$ -mercaptoethanol, heated to 95°C for 5 min, separated on NuPAGE 4%–12% Bis-Tris Gels for 90 minutes at 100 V and blotted onto Immobilon-FL PVDF membranes. The transfer was performed at a constant voltage of 30 V for 30 min. After the transfer, the membrane was blocked in 1% Casein in PBS. Proteins were stained with primary antibodies, and subsequently Infrared Dye labeled secondary antibodies, diluted in 0.05% Casein in PBS. Band intensities were quantified using Image Studio lite and protein levels were normalized on  $\beta$ -actin or GAPDH levels.

### Immunofluorescence

HeLa GL cells were grown on coverslips in 24-well plates and transiently transfected using TransIT-LT1. The cells were fixed using 4% paraformaldehyde, and permeabilized and blocked with PBS containing 0.5% Triton X-100 and 5% FBS. The cells were stained using primary antibodies, fluorescently labeled secondary antibodies, and DAPI to stain nuclei. The coverslips were mounted on microscope slides using mowiol mounting medium (10% (w/v) Mowiol 4-88, 25% (w/v) Glycerol, 25% (v/v) water, 50% (v/v) Tris-Cl 0.2M pH 8.5, 2.5% (w/v) DABCO). Images were acquired using a Zeiss LSM710 and analyzed with Fiji ImageJ. Co-localization was determined with the Huygens Professional 19.04 software.

### Autophagy quantification by counting

HeLa GL cells were grown on coverslips in 24-well plates and transiently transfected using TransIT-LT1. The cells were treated and stained for the transfected proteins as described in the Immunofluorescence method-paragraph. After acquiring images of 30+ transfected cells, the total pixel area of GFP-LC3B puncta per cell was quantified using Fiji ImageJ as previously described (Koepke et al., 2020). In brief, the channels were separated to work with the GFP-channel, the background removed and smoothed, and a threshold was applied to isolate the GFP-LC3B puncta. By analyzing the particles, the total area was determined. Cells treated with 1  $\mu$ M chloroquine overnight were used as positive control.

### Quantification of autophagosome acidification by flow cytometry

To quantify autophagosome acidification by flow cytometry, HEK293T cells stably expressing mCherry-eGFP-LC3B (HEK293T mGL) were transiently transfected using PEI. 48 h post-transfection, cells were harvested in PBS and treated for 20 min at 4°C with PBS containing 0.05% saponin. Non-membrane bound mCherry-eGFP-LC3B was washed out of the permeabilized cells using PBS twice, followed by fixation in 4% paraformaldehyde. The fluorescence intensity of membrane associated mCherry and eGFP was then quantified via flow cytometry (Cytotflex, Beckman Coulter). The quotient of the eGFP MFI/mCherry MFI was calculated. Cells treated with 100 nM Bafilomycin A1 for 8 h were used as positive control.

### Quantification of acidic organelles by flow cytometry

HEK293T cells were transiently transfected using PEI. 48 h post-transfection, the cells were treated with 100 nM LysoTracker Deep Red for 2 h. The cells were harvested in PBS and re-suspended in PBS with 1% FBS. Immediately after harvesting, fluorescence intensity of the LysoTracker Deep Red was quantified via flow cytometry (FACSCanto II, BD Biosciences). The LysoTracker Deep Red mean fluorescence intensity of the control (baseline) was subtracted. Cells treated with 100 nM Bafilomycin A1 for 4 h were used as positive control.

### Quantification of total and acidified autophagosomes by counting

HEK293T mGL cells were grown on coverslips, coated with poly-L-lysine, in 24-well plates and transiently transfected using PEI. The cells were treated and stained for the transfected proteins as described in the Immunofluorescence method-paragraph. After acquiring images of 30+ transfected cells, fluorescent puncta in the cells were counted. Here, puncta displaying both eGFP and mCherry fluorescence (non-acidified autophagosomes) and puncta displaying only mCherry fluorescence (acidified autophagosomes) were counted separately. The sum of both was calculated for the total number of autophagosomes per cell. Cells treated with 100 nM Bafilomycin A1 for 8 h were used as positive control.

### RT-qPCR

SARS-CoV-2 N (nucleoprotein) transcript levels were determined as previously described (Bozzo et al., 2020; Nchioua et al., 2020). In brief, supernatants were collected from SARS-CoV-2 infected Calu-3 cells 48 h post-infection. Total RNA was isolated using the Viral RNA Mini Kit according to the manufacturer's instructions. RT-qPCR was performed as previously described using TaqMan Fast Virus 1-Step Master Mix and an OneStepPlus Real-Time PCR System (96-well format, fast mode). Synthetic SARS-CoV-2-RNA or RNA isolated from BetaCoV/France/IDF0372/2020 viral stocks quantified via this synthetic RNA (for highly concentrated samples) were used as a quantitative standard to obtain viral copy numbers.

For the determination of IFN- $\beta$  levels of cells infected with SeV or IFNAR1 levels in cells expressing SARS-CoV-2 NSP14 or IAV HA, total RNA was extracted 24 h posts infection or 48 h post transfection respectively using the Quick-RNA Microprep Kit according to the manufacturer's instructions. Reverse transcription and qRT-PCR were performed in one step using the SuperScript III Platinum Kit on a StepOnePlus Real-Time PCR System according to the manufacturer's instructions. TaqMan probes for each individual gene were acquired as premixed TaqMan Gene Expression Assays and added to the reaction. Expression levels for each target gene were calculated, e.g., for IFNAR1 expression levels by normalizing to GAPDH RNA levels using the  $\Delta\Delta$ CT method.

### Legendplex ELISA

The Legendplex ELISA was performed according to the manufacturer's instructions. In brief supernatants of cells infected with SeV were collected 24 h post infection and incubated for 2 h at room temperature with antibody-coated beads, followed by washing and incubation with the detection antibodies. After incubation with the staining reagent, the beads were analyzed in a high-throughput sampler via flow cytometry (FACSCanto II, BD Biosciences). Absolute quantification was performed using a standard and the Biolegend Legendplex v8.0 software.

### Inhibition of SARS-CoV-2 by immune modulation

300,000 Calu-3 cells were seeded in 12-well plates. The cells were stimulated with increasing amounts of IFNs ( $\alpha$ 2,  $\beta$  and  $\gamma$ , 0.8, 4, 20, 100 and 500 U/ml or  $\lambda$ 1, 0.16, 0.8, 4, 20 and 100 ng/ml) at 24 h and 72 h post-seeding, with an intermediate medium change at 48 h post-seeding. 2 h after the second stimulation, the cells were infected with SARS-CoV-2 (MOI 0.05) with a subsequent medium change after 6 h. 48 h post-infection, cells were harvested for further analysis.

### Propagation of SARS-CoV-2

SARS-CoV-2 isolates were propagated by infecting 70% confluent Vero E6 in 75 cm<sup>2</sup> cell culture flasks at a MOI of 0.003 in 3.5 mL serum-free medium containing 1 μg/mL TPCK-treated trypsin (Sigma). The cells were then incubated for 2 h at 37°C, before adding 20 mL medium containing 15 mM HEPES. Three days post-infection, the medium was exchanged and the supernatants were harvested 5 days post-infection upon visible cytopathic effect. The supernatants were cleared by centrifugation, aliquoted and stored at –80°C. The infectious virus titer was determined as plaque forming units (PFU).

### Proteome analysis

For the proteome analysis of infected cells, 0.6x10<sup>6</sup> Caco-2 cells were infected with SARS-CoV-2 BetaCoV/Netherlands/01/NL/2020 at an MOI of 0.5 and harvested 24 h and 48 h post-infection in TM lysis buffer, supplemented with 1:500 protease inhibitor. After centrifugation for 10 min at 20,000 g and 4°C, supernatants were mixed with 6x Protein Sample Loading Buffer (at a final dilution of 1x) supplemented with 15% β-mercaptoethanol and stored at –20°C until further analysis. The samples were heated to 95°C for 10 min. For the proteome analysis of single overexpressed SARS-CoV-2 proteins, 1x10<sup>7</sup> HEK293T cells were transfected with the respective constructs (pCG vectors containing V5 tagged, codon optimized open reading frames (Orfs) of SARS-CoV-2 (Nsp1, Nsp7, Nsp15, Nsp16, S, E, M, N, ORF3a, ORF6, ORF7a)) with TransIT-LT1. The cells were harvested in PBS and processed for LC-MS using the iST-kit as recommended by the manufacturer. For LC-MS purposes, desalted peptides were injected in a nano-Elute system (Bruker) and separated in a 25-cm analytical column (75 μm ID, 1.6 μm C18, IonOpticks) with a 100-min gradient from 2 to 37% acetonitrile in 0.1% formic acid. The effluent from the HPLC was directly electrosprayed into a hybrid trapped ion mobility-quadrupole time-of-flight mass spectrometer (timsTOF Pro, Bruker Daltonics, Bremen, Germany) using the nano-electrospray ion source at 1.4 kV (Captive Spray, Bruker Daltonics). The timsTOF was operated at 100% duty cycle in data dependent mode to automatically switch between one full TIMS-MS scan and ten PASEF MS/MS scans in the range from 100–1700 m/z in positive electrospray mode with an overall acquisition cycle of 1.23 s. The ion mobility was scanned from 0.6 to 1.60 Vs/cm<sup>2</sup> with TIMS ion charge control set to 5e<sup>4</sup>, RF potential of 300 Vpp. The TIMS dimension was calibrated linearly using four selected ions from the Agilent ESI LC/MS tuning mix [m/z, 1/K0: (322.0481, 0.7318 Vs cm<sup>–2</sup>), (622.0289, 0.9848 Vs/cm<sup>2</sup>), (922.0097, 1.1895 Vs/cm<sup>2</sup>), (1221.9906, 1.3820 Vs/cm<sup>2</sup>)]. The mass spectrometry proteomics data have been deposited to the ProteomeXchange Consortium via the PRIDE partner repository with the dataset identifier PRIDE: PXD021899. MaxQuant 1.6.15.0 was used to identify proteins and quantify by LFQ with the following parameters: Database, Uniprot\_AUP000005640\_Hsapiens\_20200120.fasta supplemented with the sequences of NSP1\_V5, NSP7\_V5, NSP15\_V5, NSP16\_V5, E\_V5, M\_V5, N\_V5, S\_V5, ORF3\_V5, ORF6\_V5, ORF7\_V5 and Spike protein from SARS-CoV2 (Gordon et al., 2020); MS tol, 10 ppm; MS/MS tol, 20 ppm Da; Peptide FDR, 0.1; Protein FDR, 0.01 Min. peptide Length, 7; Variable modifications, Oxidation (M); Fixed modifications, Carbamidomethyl (C); Peptides for protein quantitation, razor and unique; Min. peptides, 1; Min. ratio count, 2. Identified proteins were considered as differential if their MaxQuant LFQ values. Raw data was analyzed using R. Outliers (below 0.05 and above 0.95) appearing in more than 2 cases were removed as artifacts of the overexpression. Heatmaps were generated using R, using the inbuilt hierarchical clustering of heatmap.2 and displayed in Corel Draw.

### GO Analysis

From the proteome of the respective samples, proteins regulated more than 4-fold compared to the vector control were extracted and submitted to PANTHER (cellular component analysis).

### Half-life analysis

We focused the half-life comparisons to proteins for which we identified peptides that resided within the first 50 N-terminal amino acids. To do this, we extracted peptides for both NSP1+ (NSP overexpression) and WT (wild-type) samples that fall within the first 50 AA window starting at the N terminus from the result file (peptide.txt, Maxquant 1.6.15.0). These peptides were then mapped to the corresponding protein intensities and the relative changes of log<sub>2</sub> transformed iBAQ values calculated and grouped into three groups: I. enriched in NSP1+: log<sub>2</sub>(fc) > 2, II. enriched in WT: log<sub>2</sub>(fc) < –2, III. Not enriched: –2 ≤ log<sub>2</sub>(fc) ≤ 2. For proteins, where data on the half-lives of in hepatocytes (Mathieson et al., 2018) was available, these data were extracted and plotted by scaling their mean half-lives corresponding to the proteins in each group to the interval [0–1] using min-max normalization and generated boxplots for each of them. MATLAB 2019b was used for the half-life analysis.

### QUANTIFICATION AND STATISTICAL ANALYSIS

Statistical analyses were performed using GraphPad PRISM 8. P values were determined using a two-tailed Student's t test with Welch's correction. Unless otherwise stated, data are shown as the mean of at least three biological replicates ± SEM. Significant differences are indicated as: \*, p < 0.05; \*\*, p < 0.01; \*\*\*, p < 0.001. Not significant differences are not indicated. Statistical parameters are specified in the figure legends.